Renewable Energy 260 (2026) 124977

Contents lists available at ScienceDirect

Renewable Energy

journal homepage: www.elsevier.com/locate/renene

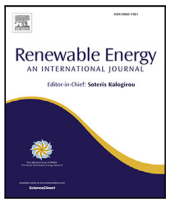

Unsteady aerodynamics of large-scale floating offshore wind turbines in surge motion

Christian W. Schulz [a,*], Roger Bergua [b], Emmanuel Branlard [c], Stefan Netzband [a], Jason Jonkman [b], Amy Roberston [b]

[a] Hamburg University of Technology, Hamburg, 21073, Germany
[b] National Wind Technology Center, National Renewable Energy Laboratory, Golden, CO 80401, USA
[c] University of Massachusetts Amherst, Amherst, A 01003, USA

ARTICLE INFO

Keywords:
Floating wind
FOWT
Unsteady aerodynamics
Returning wake
Surge motion
IEA 15-MW

ABSTRACT

Unsteady aerodynamic loads significantly influence the design and wake flow field of floating offshore wind turbines, especially due to wave- or vibration-induced tower top motions triggering various unsteady phenomena. Recent studies show that increasing turbine sizes amplify unsteady aerodynamic effects, as their impact typically grows with rotor diameter. This work combines recent findings from experiments and simulations on model-scale FOWT aerodynamics with new numerical analyses of large-scale rotors, providing a comprehensive understanding of unsteady phenomena occurrence and impact. Numerical analyses of the IEA 15-MW and 22-MW rotors undergoing surge motions characterise the combined influence of motion-induced unsteady phenomena on rotor thrust. Results indicate that unsteady effects can reduce thrust force variations by up to 40% at realistic surge periods. These findings contrast with prior model-scale rotor investigations, attributed to the specialised design of the model rotors. Comparisons between numerical methods — the dynamic blade element momentum method in OpenFAST and free vortex wake modules in *pan*MARE and OpenFAST — reveal persistent differences in thrust predictions under both idealised and realistic conditions. This highlights that classical blade element momentum approaches require enhancement to accurately capture unsteady loads on large-scale floating offshore wind turbines at low wind speeds.

1. Introduction

Floating offshore wind turbines (FOWT) are an emerging technology with the potential to harness a large amount of wind energy in deep-water locations. Accurately predicting the aerodynamic loads on these turbines, taking platform motions due to wave excitation into account, is essential for designing turbines that use resources efficiently. In addition, the precise prediction of rotor loads is a prerequisite for modelling the wake flow field and its recovery, which is potentially enhanced by tower top motions [1,2]. Although numerous studies have been performed in this field, a general understanding of how and which unsteady aerodynamic phenomena affect the loads on a moving wind turbine rotor is still lacking. The present work aims at closing this knowledge gap by extending prior investigations on model-scale rotors to large-scale rotors and generalising the findings to draw a clear picture of unsteady phenomena caused by surge motions.

An attempt to identify the relevant unsteady aerodynamic phenomena was recently made by some of the authors [3]. The analysis in [3] is based on the idea that the load fluctuations caused by platform motions can be described in terms of a quasi-steady and an unsteady part. The present work follows this fundamental idea: The quasi-steady part of the load response corresponds to the change of the actual inflow conditions (i.e. relative inflow velocity and tip speed ratio (TSR)). It usually dominates the load response in the case of a tower top motion parallel to the wind speed (i.e. platform surge or pitch motion). The unsteady part can be interpreted as a perturbation on the quasi-steady response caused by different unsteady phenomena. Experiments performed in the previous study revealed no influence of unsteady effects on the rotor loads during surge motions for the considered motion frequency range. However, free vortex wake (FVW) simulations exceeding the motion frequency range of the experiment predicted the occurrence of the unsteady airfoil effect and returning wake effect and hinted to the presence of the dynamic wake effect. The returning wake effect has been discovered in the context of helicopter aerodynamics, and its occurrence in the context of FOWT under wave-induced motions was demonstrated for the first time in [3]. These findings extend the knowledge gained in an extensive validation and verification study on

* Corresponding author.
E-mail address: christian.schulz@tuhh.de (C.W. Schulz).

https://doi.org/10.1016/j.renene.2025.124977
Received 29 July 2025; Received in revised form 5 December 2025; Accepted 5 December 2025
Available online 15 December 2025

Nomenclature

Abbreviations	
(D)BEM	(Dynamic) blade element momentum
FOWT	Floating offshore wind turbine
FVW	Free vortex wake
IEA	International Energy Agency
LES	Large-eddy simulation
NREL	National Renewable Energy Laboratory
OC6	Offshore Code Comparison Collaboration, Continued, with Correlation and unCertainty
*pan*MARE	Panel Code for Marine Applications
RAO	Response amplitude operator
TUHH	Hamburg University of Technology
TSR	Tip speed ratio
VRS	Vortex ring state
Symbols	
a	Axial induction factor
A_L	Lift force amplitude
$A_{L,qs}$	Quasi-steady part of A_L
A_T	Thrust force amplitude
$A_{T,qs}$	Quasi-steady part of A_T
A_T^*	A_T normalised by $A_{T,qs}$
$\Delta A^*_{\text{T, dyn. wake}}$	Part of A_T^* attributed to the dynamic wake effect
$\Delta A^*_{\text{T, ret. wake}}$	Part of A_T^* attributed to the returning wake effect
c	Chord length
C_t	Thrust coefficient
D	Rotor diameter
f	(Surge) motion frequency
f_a	Airfoil reduced frequency
f_p	Motion to blade-passing frequency ratio
f_r	Rotor reduced frequency
H_s	Significant wave height
m	An integer value
n_b	Number of blades
$P(f_a, f_p)$	Unsteady perturbation function of A_L
r	Radial coordinate
R	Rotor radius
T	Thrust force
$\Delta T_{\text{unsteady}}$	Part of the thrust force amplitude caused by unsteady phenomena
T_p	Peak period
v_0	Wind velocity
v_{in}	Actual inflow velocity seen by the rotor
v_{ind}	Axial induced velocity
Δv_{ind}	Difference of v_{ind} during forward and backward motion
Δv^*_{ind}	Δv_{ind} normalised (by the no-motion condition)
$\Delta v^*_{ind,qs}$	Quasi-steady part of Δv^*_{ind}
V_m	Surge motion velocity amplitude
ΔV^*	Normalised motion velocity amplitude
α	Angle of attack
λ	Tip speed ratio
Ω	Angular frequency of the rotor
ρ	Air density

the UNAFLOW model rotor undergoing surge motions, which was performed during International Energy Agency (IEA) Task 30 / OC6[1] Phase III [4]. It has to be noted that both studies focused on the identification of the basic unsteady phenomena and therefore considered simplified setups excluding turbine control. Since scientific developments in this field are crucial, two relevant experimental studies and a number of numerical investigations have emerged recently. These works are described briefly, while a more comprehensive literature review can be found in [3].

The first experiment is a new test campaign of the UNAFLOW rotor in motion focusing on wake dynamics conducted by Fontanella et al. [5]. In addition to the investigation of the wake, rotor thrust and torque measurements were performed and an inertia compensation strategy was applied to remove the inertia loads from the measurements. From previous studies using the UNAFLOW rotor, a linear trend between the thrust force amplitude normalised by the platform motion amplitude and the motion frequency would be expected. However, during these experiments a slight deviation of the normalised thrust amplitude at high motion frequencies (rotor reduced frequency $f_r = 1.2$, see Eq. (6)) in surge and pitch motion cases was observed. In case of the pitch motion, where the increase of the thrust amplitude was strongest, a large scattering of the results persists. Fontanella et al. [5] attribute the deviation from the linear trend to inaccuracies of the measurement setup, namely, rotor speed variations and tower vibrations. This interpretation is in line with the experimental results in the abovementioned study [3], where the rotor torque of the TUHH (Hamburg University of Technology) model turbine was instigated in a similar range of rotor reduced frequencies (f_r between 0.55 and 1.09), and no hint on a deviation from the quasi-steady behaviour was found.

The second experiment focused on the measurement of the thrust force of a model turbine during harmonic surge, pitch and yaw motions and was conducted by Taruffi et al. [6]. For surge motions with rotor reduced frequencies between 0.15 and 0.9, the thrust force amplitude scatters in a range of 80 to 100% of the quasi-steady reference. A sudden increase of 30 to 70% of the amplitude was observed at $f_r = 1.5$ for a number of different motion velocity amplitudes. This increase is attributed to the presence of unsteady aerodynamic phenomena by the authors. In a follow-up study, results from large-eddy simulations (LES) combined with an actuator line approach were compared to selected measurements [7]. The simulations were unable to reproduce the sudden increase of the thrust force amplitude. Taruffi et al. [7] conjectured that the unsteady phenomena were caused by airfoil-level aerodynamics which could not be resolved by the actuator line formulation. Similarly, other numerical studies using different methods and rotors did not show a significant increase of the thrust force amplitude at the corresponding rotor reduced frequencies (e.g. [3,8–10]). Therefore, it is of major interest for the research community to determine whether the measurements of Taruffi et al. [6] can be reproduced in a different setup in the future.

The explicit numerical analysis of unsteady aerodynamic phenomena in the context of a moving rotor was in focus of three recent studies [9,11,12]. In the one of the studies, Zhou et al. [11] investigated the behaviour of the National Renewable Energy Laboratory (NREL) 5-MW rotor using a (lifting-line) FVW method with an in-house implementation of the Leishman–Beddoes unsteady airfoil model [13]. It was found that there is an increasing phase lag between the rotor loads and the surge motion with increasing motion frequencies at moderate motion amplitudes (where dynamic stall is of minor relevance). This is in line with findings from several studies (e.g. [3,4]). While it is common sense that the unsteady airfoil effect contributes to this phase shift, it is still not fully understood if there is a contribution of the dynamic wake effect.

The other two studies by Papi et al. [9] and Sanvito et al. [12] extended the simulation study of the UNAFLOW rotor from OC6 Phase III. The motion frequencies were increased up to 16 Hz ($f_r = 9.09$). Both could reproduce the presence of the returning wake effect found for the same rotor and motion frequencies in [3]. Sanvito et al. [12] used an actuator line method while Papi et al. [9] performed actuator line, FVW

[1] Offshore Code Comparison, Collaboration, Continued, with Correlation and uncertainty.

and dynamic blade element momentum (DBEM) theory simulations. The normalised thrust amplitudes of all three studies agree closely. Sanvito et al. [12] kept the motion velocity amplitude constant and varied the motion frequency of the rotor in order to distinguish between quasi-steady and unsteady parts of the thrust response. Papi et al. [9] compared the thrust amplitudes at different motion frequencies to an empirical quasi-steady reference to identify such unsteadiness similar to the one used by Taruffi et al. [6]. Both studies also investigated the phase shift between the surge position and the thrust force and found an increasing magnitude of the phase shift up to the point where the motion frequency equals the 3P frequency and a sharply decreasing phase shift for higher motion frequencies. Comparable results were found by Schulz et al. [3], but an error in post-processing led to higher peaks being reported at higher motion frequencies.

In addition, the distribution of the axial induction over the blade during the surge motion cycle was analysed in the two recent numerical studies. As indicated by Ferreira et al. [14], the choice of the reference frame has a major influence on the calculated axial induction factor, and the absolute reference frame is considered to be the correct one. Therefore, Sanvito et al. [12] define an absolute axial induction based on the absolute reference frame and Papi et al. [9] directly consider the absolute induced velocity. Papi et al. [9] found that the dynamic inflow model in the DBEM simulations reduces the fluctuation of the induced velocity caused by the surge motion. This is in line with theoretical expectations as the dynamic wake effect acts as a low-pass filter on the induced velocity. However, no impact of this effect could be identified in the total thrust force response. Papi et al. [9] argue that the impact of the attenuation of the induced velocity in the inner and the outer blade regions compensate each other due to their 180° phase shift. Sanvito et al. [12] found that the amplitude of the absolute axial induction significantly increases when the surge motion reaches the 3P frequency. At first glance, this seems to be a contradiction to the expected behaviour of the dynamic wake effect and the observations by Papi et al. [9]. The current authors believe that this issue is not of physical nature but a matter of definition of the induced velocity, which is discussed in Section 4.4 later in this work. Furthermore, all three studies as well as previous works find that the dynamic wake effect does not alter the thrust or torque amplitude in case of the UNAFLOW rotor. In contrast to this, a clear indication that the load amplitude of the IEA 15-MW rotor is affected by this effect was found by Schulz et al. [3]. This apparent contradiction will also be investigated in Section 4.4.

Scope of work

The present work attempts to improve the general understanding of the unsteady aerodynamic phenomena in the context of FOWT by addressing the following goals:

- Characterisation of the impact of the relevant unsteady phenomena (dynamic wake, unsteady airfoil and returning wake effect) on the thrust force response to tower top surge motions of the IEA 15-MW and IEA 22-MW wind turbine rotors based on DBEM and FVW simulations.
- Generalisation of the principal unsteady behaviour of a wind turbine rotor in surge motion by a thrust force response characteristic based on suitable dimensionless numbers.
- Provision of an explanation for the unexpected absence of the dynamic wake effect in model-scale by an investigation of the induced velocity.
- Demonstration of the applicability of the generalised thrust response characteristic and the significant impact of the returning wake effect under realistic conditions.
- Investigation of the impact of modelling fidelity on the simulation of the unsteady aerodynamic phenomena.

FVW and DBEM simulations using the codes *pan*MARE and OpenFAST (described in Section 3) are used to characterise the unsteady phenomena acting on the considered turbines. In Section 4, the dedicated load cases proposed in the previous work [3] are adopted to the larger rotors in order to identify the unsteady contributions. In Section 4.3, the impacts of the three unsteady effects are summarised in the generalised thrust response characteristic. Finally, the occurrence of the returning wake effect under realistic motions generated by coupled simulations of the 22-MW semi-submersible FOWT is demonstrated in Section 5 and the most relevant conclusions are drawn in Section 6.

2. Fundamentals

2.1. Thrust force response to tower top surge motions

A wind turbine's response to a surge motion can be considered as unsteady. This is due to the fact that the flow situation seen by the rotor changes progressively. Nevertheless, such response can be expressed in a *quasi-steady* manner, when the movement is sufficiently slow. In contrast to this, fast motions presumably trigger unsteady aerodynamic phenomena that additionally influence the rotor loading. In the following, this kind of behaviour is denoted as *unsteady*, which excludes quasi-steady effects. Considering a pure, harmonic surge motion with a velocity amplitude V_m, the resulting relative inflow velocity v_{in} acting on a rotor in a uniform wind field (v_0) becomes

$$v_{\text{in}} = v_0 - V_m \cos(2\pi f t). \tag{1}$$

With the normalised motion velocity amplitude[2] ΔV^*, defined as:

$$\Delta V^* = \frac{V_m}{v_0}, \tag{2}$$

the amplitude of the thrust force response A_T to such motion at constant rotational speed can be written as follows (see [3]).

$$A_T = \underbrace{\frac{\rho R^2 \pi v_0^2}{2} \frac{1}{2} \left(C_t\left(\lambda_{\min}\right)(1+\Delta V^*)^2 - C_t\left(\lambda_{\max}\right)(1-\Delta V^*)^2 \right)}_{\text{quasi-steady}} + \underbrace{\Delta T_{\text{unsteady}}}_{\text{unsteady}} \tag{3}$$

In Eq. (3) R, ρ and v_0 describe the rotor radius, the air density and the wind velocity parallel to the rotor axis, respectively. The thrust coefficient C_t is determined by the TSR, which reaches its minimum, $\lambda_{\min}$, during the forward motion, where v_{in} is highest, and its maximum, $\lambda_{\max}$, during the backward motion, where v_{in} is smallest. The first part of the equation describes the quasi-steady load response, while $\Delta T_{\text{unsteady}}$ summarises all contributions to the thrust force amplitude that arise from unsteady phenomena. Consequently, the thrust force amplitude can be determined from the quasi-steady part alone in case of a motion with a very high period, for which $\Delta T_{\text{unsteady}}$ tends to zero.

The minimum and maximum TSRs can be resolved in terms of ΔV^*:

$$\lambda_{\min} = \frac{R\Omega}{v_0(1+\Delta V^*)} \text{ and } \lambda_{\max} = \frac{R\Omega}{v_0(1-\Delta V^*)}, \tag{4}$$

where the rotational speed is denoted as Ω. Finally, the quasi-steady part of the thrust force amplitude A_T is completely determined by ΔV^*, because $\lambda_{\min}$ and $\lambda_{\max}$ are only dependent on ΔV^* when the rotational speed is constant. As the quasi-steady part typically dominates the load response (see Section 1), the normalised motion velocity amplitude ΔV^* is most relevant to determine this response. However, it does not contain any information on the degree of unsteadiness that can be expected.

[2] This parameter was introduced as b_{vel} in [3].

2.2. Unsteady phenomena

The most significant unsteady aerodynamic phenomena arising for a typical FOWT in moderate tower top surge motions are the unsteady airfoil, the dynamic wake (or dynamic inflow) and the returning wake effects. Only a very brief summary of these effects is given in the following, while a more detailed description in the context of surge motions can be found in [3].

The unsteady airfoil effect summarises the impact of vortices shed from the trailing edge on the inflow of the airfoil (circulatory part) and added mass effects (non-circulatory part). The latter arise from the unsteady displacement of the air around the accelerated airfoil. Both parts are attached flow phenomena and can be described by thin-airfoil theory (e.g. Theodorsen's theory). The unsteady airfoil effect can be characterised by the *airfoil reduced frequency* f_a defined by Sebastian and Lackner [15] for every radial station of the blades:

$$f_a = \frac{\pi f c(r)}{\sqrt{v_0^2 + (r\Omega)^2}}. \tag{5}$$

where f is the motion frequency, r is the radius and c denotes the chord length of the considered radial section, respectively. The unsteady airfoil effect can be related to *dynamic stall*. However, the stalled blade regions do not contribute significantly to the overall rotor thrust force of large-scale wind turbines in normal operation (below-rated) and at typical motion conditions. Therefore, dynamic stall is excluded from the following analysis and not discussed here.

The dynamic wake effect captures the fact that a distinct time is needed for the wake to propagate and reach a steady state after a change of rotor loading (or rotor circulation). Therefore, the induced velocities at the rotor, which are mainly due to the trailing vortices of the wake (e.g. tip and root vortices), also changes progressively according to the time constant of the wake propagation. This time constant can be characterised by the *rotor reduced frequency* f_r:

$$f_r = \frac{f D}{v_0} \tag{6}$$

where D describes the rotor diameter.

The returning wake effect describes the impact of shed vorticity[3] from one blade to another. It develops its maximum impact on the rotor loads when the surge motion frequency f is a multiple of the blade passing frequency (3P for a three-bladed rotor) and can therefore be characterised by the *motion to blade-passing frequency ratio* f_p introduced in [3]:

$$f_p = \frac{2\pi f}{n_b \Omega}, \tag{7}$$

where n_b denotes the number of blades. It has to be noted that both, the (circulatory) unsteady airfoil and the returning wake are caused by the same vortices shed from the trailing edge. As a consequence, the presence of the unsteady airfoil effect is a prerequisite for the returning wake effect.

In some studies, the occurrence of blade-wake interactions is analysed (e.g. [16] or [9]). However, these studies employ quite extreme motion conditions (e.g. a normalised motion velocity amplitude ΔV^* of 100% and more), which are relatively uncommon. The same applies for the occurrence of a vortex ring state (VRS) or a propeller state during operation[4] (e.g. [17,18] or [16]).

[3] Vortices that are shed parallel to the trailing edge of the airfoil.

[4] Ferreira et al. [14] argue that the occurrence of a VRS is often predicted erroneously, because the moving reference frame instead of the absolute reference frame is applied to evaluate the state of the stream tube. Papi et al. [9] follow this reasoning and show that even in extreme cases, no flow reversal can be detected in the absolute reference frame, which is considered to be the correct one when evaluating the state of the stream tube. Papi et al. [9] show that although VRS does not occur, a blade-wake interaction might be possible in extreme cases. However, for a 15-MW semi-submersible FOWT, it is estimated that a wave height of 10–13 m with wave periods between 7.7 and 11.1 s and a wind velocity of 5 m/s resulting in $\Delta V^* = 87\%$ is required to reach such conditions, which is an extremely seldom case.

2.3. Typical motion conditions

The platform motions of FOWT are surge, heave, sway, pitch, roll and yaw motions. When transferred to the reference frame of the rotor, all platform motions can be represented as a combination of tower top[5] translations and rotations (i.e. a platform pitch motion can be expressed as a tower top surge motion and a rotation of the rotor around the tower top). A number of studies show that the power and thrust of a rotor is much less sensitive to sway or yaw motions compared to pitch and surge motions (e.g. [19] or [5]). When assuming a uniform inflow, the finding for the sway motion can be generalised to any lateral motion in the rotor plane and is therefore also valid for heave motions. Similarly, a rotation around the yaw axis is approximately equivalent to the rotational part of a platform pitch motion in the rotor reference frame. Consequently, sway and heave motions as well as pure tower top rotations in any direction do not cause significant changes of the overall rotor power and thrust.[6] In contrast to this, tower top motions in surge direction (parallel the wind direction) cause the most relevant fluctuations of thrust and torque. Such motions can be caused by platform surge and pitch motions, since both cause a longitudinal motion of the tower top in wind direction.

Tower top surge motions can be caused by wave-induced platform motions and structural (tower) vibrations.[7] The wave forcing typically is in a range from 5 to 20 s,[8] while tower vibrations occur at lower periods, typically up to 5 s. Typical response amplitude operators (RAOs) of spar and semi-submersible FOWT usually show that non-negligible amplifications may occur in the abovementioned wave frequency region and above.[9] Platform eigenmodes may also be excited by wave forcing or turbulent winds. These motions occur at higher periods, as large-scale FOWTs are typically designed so that the natural periods in surge and pitch lie well above the dominant wave period range. However, due to nonlinearities in wave forcing, excitation can still occur from wave regimes that do not directly overlap with the platform's natural frequencies. In the case of pronounced eigenmotions induced by waves or turbulence, even longer periods may need to be accounted for. Still, it remains uncertain to what extent such motions contribute to significant tower top velocities during turbine operation.

As described in the previous paragraph, the tower top motion period corresponds to a certain rotor reduced frequency f_r for a specific rotor (i.e. rotor size and rating) and wind speed (see Eq. (6)). Therefore, a range of realistic rotor reduced frequencies can be given for a certain rotor (size) dependent on the wind speed and motion period. In

[5] Strictly speaking, motions of the rotor centre would be the correct term here, but we stick to tower top motions to maintain a more intuitive understanding.

[6] This does not necessarily apply for the loads acting on the individual blades.

[7] Hints on significant periodic tower top motions induced by aerodynamic load fluctuations have not been found in literature.

[8] Lower wave periods may occur; however, as wave height and periods are correlated, only very low wave heights below 1 m are associated with such periods. Wave periods of more than 20 s are associated with wave heights above 14 m according to IEC 61400-3-1:2019 (*Wind energy generation systems - Part 3-1: Design requirements for fixed offshore wind turbines*), which are extremely unlikely to occur when the turbine is in operation (see e.g. [20]).

[9] For spar concepts, usually a rising amplification can be seen with the motion period (see, e.g. 5-MW spar [21] and 10-MW spar [22]) for surge and pitch motions. However, at periods below 5 s hardly any surge or pitch motion can be expected. For the IEA 15-MW semi-submersible, Allen et al. [23] directly show a nacelle fore-aft motion RAO, which is most suitable for the estimation of tower-top surge motions. According to this, relevant motions can be expected at motion periods above 4.5 s.

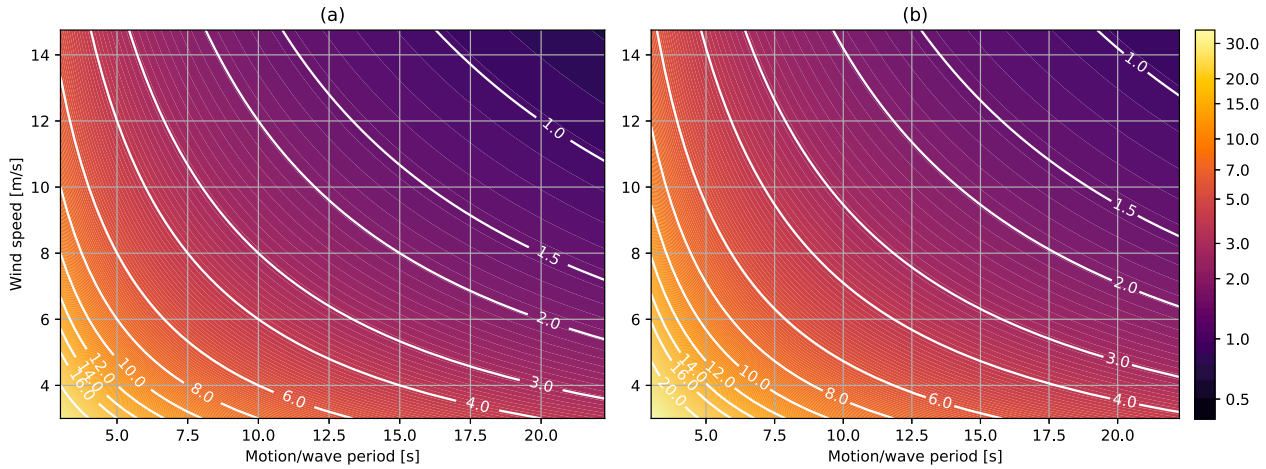

Fig. 1. Maps of rotor reduced frequencies (f_r) for the IEA 15-MW (a) and the IEA 22-MW (b) wind turbines at different wind speeds and surge motion periods. f_r increases from dark violet to yellow. Contour lines indicate absolute values of f_r.

Fig. 1(a) and (b), these ranges are given in colour maps for the IEA 15-MW and the IEA 22-MW rotors. For the IEA 15-MW rotor, realistic rotor reduced frequencies range from a bit less than 1 up to 16 near cut-in and at 5 s motion period. At an intermediate motion period of 10 s, reduced frequencies between 1.5 and 8 can be considered as realistic. Even higher reduced frequencies with values from 2 up to 10 are reached for the IEA 22-MW rotor. Knowing this, it seems that previous studies often did not cover the upper range of realistic rotor reduced frequencies properly for large-scale FOWT (see literature overview in [3]). For example, the maximum reduced frequency reached in recent experimental studies is only 1.5.

3. Numerical methods and models

The two lifting line FVW methods *pan*MARE and OpenFAST FVW (or OLAF) as well as OpenFAST DBEM are used in the following to investigate the unsteady aerodynamic phenomena relevant for FOWT rotors. Lifting line FVW methods are able to capture all unsteady phenomena based on shed and trailing vorticity intrinsically. This applies to the effects listed in Section 2 with the exception of dynamic stall and the non-circulatory part of the unsteady airfoil effect. Yet, both effects can be modelled with empirical corrections. However, they are considered to be of minor relevance as discussed above and in [3]. Therefore, in the following the term *unsteady airfoil effect* mostly refers the circulatory part of this effect, which is caused by vortex shedding from the trailing edge. Despite the fact that static, empirical airfoil polars are used by the FVW methods, this circulatory effect can be intrinsically modelled by lifting line FVW methods since the change of circulation over time is directly modelled (see [3] for a deeper discussion and demonstration).

All considered cases are additionally simulated in the widely-used DBEM method AeroDyn, which is also part of the OpenFAST framework and can be seen as a representative for the industry standard. A brief description of all three methods can be found in Appendix A.

Numerical models for the IEA 15-MW turbine are set up in *pan*MARE, OpenFAST FVW and OpenFAST DBEM separately. For the IEA 22-MW rotor, only one lifting line setup is created in *pan*MARE, as the investigations on the IEA 15-MW rotor show only marginal differences between the two lifting line solvers with regard to the unsteady load response. As the subsequent analysis shall focus on basic unsteady aerodynamic phenomena, rotor cone and tilt angles are set to zero. Concurrently, no structural flexibility and no tower are considered in the models. The description of the model setups including the configuration of the unsteady corrections is given in Appendix B.

Table 1
Comparison of steady rotor loads of the applied simulation models.

Method	TSR	Thrust coefficient		Power coefficient	
	[–]	C_t [–]	Δ DBEM [%]	C_p [–]	Δ DBEM [%]
IEA 15-MW					
OpenFAST DBEM	9.0	0.800	–	0.483	–
OpenFAST FVW	9.0	0.830	**3.7**	0.535	**10.6**
*pan*MARE FVW	9.0	0.816	**2.0**	0.510	**5.6**
IEA 22-MW					
OpenFAST DBEM	9.15	0.803	–	0.488	–
*pan*MARE FVW	9.15	0.875	**9.0**	0.500	**2.4**

3.1. Comparison of numerical models in steady conditions

A comparison of the thrust and power coefficients of the IEA 15-MW and the IEA 22-MW rotors predicted by the three different simulation methods is given in Table 1. For the IEA 15-MW rotor, three different wind speeds in the below-rated range (7 ms^{-1}, 8.5 ms^{-1} and 10 ms^{-1}) and a uniform wind field are applied. In all three cases, a constant rotational speed resulting in an optimum TSR of 9 is chosen, so that the desired operating condition defined by the control strategy is met properly. As a result of the constant TSR, thrust and power coefficients are identical for all three cases. The FVW methods predict consistently higher thrust and power coefficients, while a remarkable difference of 10.6% in power coefficient between OpenFAST FVW and OpenFAST DBEM is present. However, the generally higher loads as well as such large deviations have already been reported in previous literature (e.g. [24,25]) and can therefore be considered as a consequence of the different simulation approaches. The deviations between OpenFAST FVW and *pan*MARE can be attributed to differences in the wake treatment,[10] because different solution procedures for the circulation and blade loads are not known to lead to notable deviations of the results.

For the IEA 22-MW turbine, the optimum TSR is set to 9.15, and a blade pitch angle of −0.64 ° is applied according to the control strategy of the turbine. The deviations between the simulation approaches are comparable to those observed for the IEA 15-MW rotor, but in this case, the thrust coefficient calculated by *pan*MARE is 9% higher in comparison to OpenFAST DBEM's result. The differences observed in the steady-state responses between FVW and DBEM methods are non-negligible, but considered marginal for the purpose of this work.

[10] Both codes have different models for the convection of the wake (e.g. transitioning from free to partially frozen) and its diffusion.

Table 2
Set of simulation load cases for the IEA 15-MW and the IEA 22-MW rotors. One row covers a load case series with constant wind speed and TSR, while ranges are given for the amplitudes and periods. Motion amplitudes for the individual cases may be calculated from ΔV^* with the motion periods, which are listed below the table.

Absolute				*Dimensionless*			
Wind speed [ms^{-1}]	Rot. speed [rpm]	Period [s]	Amplitude (A) [m]	TSR [−]	f_r [−]	A/D [−]	ΔV^* [−]
IEA 15-MW							
7.0	5.01	2.5–1000[a]	0.30–140.0	9.0	13.71–0.03	0.1–58.3%	12.57%
8.5	6.09	–	–	–	11.29–0.03	–	–
10.0	7.16	–	–	–	9.60–0.02	–	–
IEA 22-MW							
5.5	3.39	2.95–2000[b]	0.33–220.0	9.15	17.50–0.03	0.1–78.6%	12.57%
7.0	4.31	–	–	–	13.75–0.02	–	–
8.5	5.23	–	–	–	11.33–0.02	–	–
10.0	6.15	–	–	–	9.63–0.01	–	–

[a] 2.5, 2.8, 3.3, 4, 5.5, 7, 10, 14, 21, 35, 70, 100, 200, 300, 500, 1000 s
[b] 2.95, 3.1, 3.25, 3.8, 3.95, 4.6, 5.9, 7, 10, 14, 21, 35, 70, 100, 200, 300, 500, 1000, 1600, 2000 s

Indeed, the following analyses strictly focus on the isolation of unsteady aerodynamic effects and are therefore insensitive to steady modelling differences between the methods.

4. Impact of unsteady phenomena on rotor thrust

4.1. Load cases

The aim of the following analysis is to identify unsteady contributions in the load response of the two rotors undergoing harmonic surge motions. For this purpose, specialised load case series are applied to isolate the impact of such phenomena from the quasi-steady effect of the varying relative inflow velocity seen by the moving rotor. The idea of these load case sets, which were proposed in [3], is to apply the same variation of the relative inflow velocity (i.e. a constant ΔV^*) to the rotor while varying the motion period. When additionally keeping the rotational speed constant, this results in the same cyclic variation of the instantaneous TSR[11] for all load cases in a series.

The selected load case series are listed in Table 2. For every load case series, the wind speed, blade pitch angle and rotational speed are constant. One line in the table describes a whole series. For all cases, a normalised motion velocity amplitude ΔV^* of 12.57% of the wind speed is chosen.[12] However, it is shown later in this work that the presented results are insensitive to ΔV^* and can therefore be transferred to any tower top surge motion condition of a FOWT in non-extreme sea states. The relative inflow velocity during one surge motion cycle is shown in Fig. 2(a) for different motion periods of the 7 ms^{-1} load case series of the IEA 15-MW rotor. All load cases are in the below-rated control region in order to exclude the influence of the blade pitch controller. Similarly, the rotational speed is kept constant for every load case series, because rotational speed variations can also lead to the occurrence of unsteady phenomena (see [10]), which may be confused with the effect of the surge motion itself. Keeping the rotational speed constant does not reflect the real behaviour of an FOWT, however, it is necessary to isolate and identify the unsteady phenomena. It has to be noted that some of the load cases are academic in nature and may not occur in reality (especially the ones with large periods). However, those are useful to understand the development of the unsteady contributions with varying motion period.

[11] The instantaneous TSR is based on the relative inflow velocity rather than only the wind speed.
[12] This is an arbitrary choice roughly meeting the tower top motion of a semi-submersible in moderate to harsh conditions at realistic wave periods.

4.2. Simulation results

Sample results of the IEA 15-MW rotor from *pan*MARE simulations for the 7 ms^{-1} wind condition are shown for selected motion periods in Fig. 2(b). The thrust force is normalised to the steady condition without surge motion. Two dashed grey lines show the results of steady *pan*MARE simulations at wind velocities of $v_0 + V_m$ and $v_0 - V_m$. These represent the quasi-steady behaviour at maximum and minimum relative inflow velocity caused by the motion. The thrust force in Fig. 2(b) follows a sinusoidal shape when undergoing the surge motions. This compares well to the behaviour of the relative inflow velocity in Fig. 2(a). In case of a motion period of 1000 s, the peak-to-peak amplitude exactly equals the difference between the steady simulations (dashed grey lines). Therefore, it is very likely that the thrust force response can be considered as quasi-steady and is determined by the first term of Eq. (3). The second term of Eq. (3), which summarises possible unsteady contributions to the thrust force amplitude, tends to zero in this case. However, with decreasing motion period, the thrust force amplitude is reduced. Since the relative inflow velocity is the same for all load cases (i.e. motion periods), it can be concluded that this reduction is caused by unsteady aerodynamic phenomena. It is remarkable that this can already be noticed for a motion period of 200 s, which corresponds to approximately 17 full rotor rotations and is far slower than a wave-induced motion.

In order to visualise the impact of the unsteady effects more systematically, Fig. 3 shows the thrust force amplitudes in absolute numbers over the motion period. The x-axis is displayed with a logarithmic scale in order to resolve the wave frequency region properly while including the extremely large periods. The results of all three simulation methods are shown. At the largest period of 1000 s, the thrust force amplitude can be considered as approximately quasi-steady. The obvious differences between the results at this period are therefore caused by differences of the steady modelling of the simulation methods and setups. As mentioned in Section 3.1, such differences are relevant to determine the overall load response, but do not provide insights into the unsteady behaviour of the turbine. The impact of unsteady aerodynamic phenomena on the results, however, can be observed by the change of the thrust amplitude from large to small periods. In order to highlight these changes, the thrust force amplitudes A_T are normalised to the quasi-steady amplitude $A_{T,qs}$ in Fig. 4. The normalisation can be expressed as follows:

$$A_T^* = \frac{A_T}{A_{T,qs}}. \tag{8}$$

$A_{T,qs}$ is determined by means of the thrust force T in steady simulations with maximum and minimum relative inflow velocities during the motion cycle:

$$A_{T,qs} = \frac{1}{2}\Big(T(v_{\text{in}} = v_{\text{max}}) - T(v_{\text{in}} = v_{\text{min}})\Big) \tag{9}$$

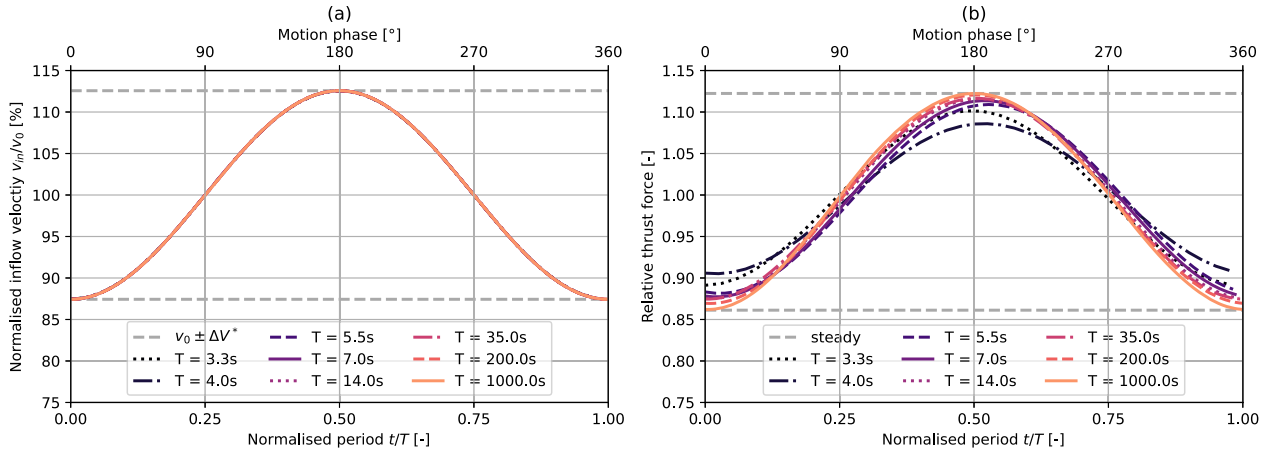

Fig. 2. Illustration of relative inflow velocity (a) and rotor thrust force (b) of the IEA 15-MW rotor during selected surge motions from Table 2. The thrust force is obtained by *pan*MARE FVW simulations. Dashed grey lines indicate steady results at minimum and maximum relative inflow velocity.

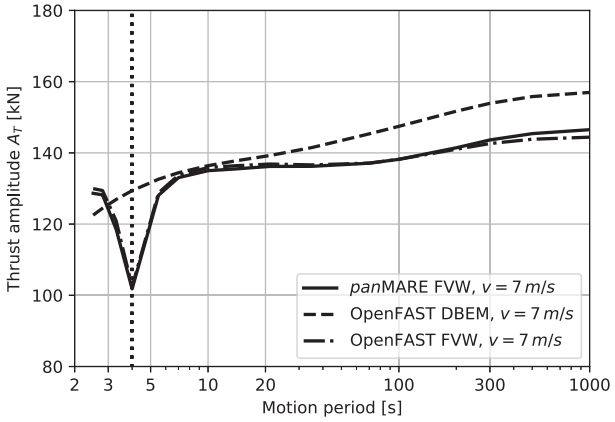

Fig. 3. Rotor thrust force amplitude of the IEA 15-MW rotor for varying surge motion periods as defined in Table 2 for the 7 ms^{-1} wind condition. Results are obtained by all three simulation methods. The x-axis is displayed in a logarithmic manner. The dotted vertical line indicates $f_p = 1$ i.e. the motion frequency equals the blade passing frequency.

where

$$v_{\max} = v_0 + V_m;\ v_{\min} = v_0 - V_m. \tag{10}$$

As $A_{T,qs}$ is calculated individually for every method, the normalised thrust force amplitude A_T^* is unity when there is no difference to the quasi-steady case. Opposite to this, differences from unity indicate the presence of unsteady phenomena.[13] It is therefore evident that the sudden minima predicted by the FVW methods in Fig. 4 (b, c and e) represent unsteady behaviour. The minima occur exactly at the dotted vertical lines, which mark the 3P blade passing frequency for the different load case series. Consequently, the motion to blade passing frequency ratio f_p equals 1 at the marked periods. The occurrence of the minima at $f_p = 1$ is in line with the findings previously published in [3] and can therefore be assigned to the presence of the returning wake effect. Since returning wake effect and (circulatory) unsteady airfoil effect occur simultaneously, a distinction of their individual impact on the FVW results is difficult. However, the impact of the isolated unsteady airfoil effect can be observed in the OpenFAST DBEM results in Fig. 4(a) and (d), because the returning wake effect is not modelled in this method. It causes a decrease of the thrust force amplitude at periods lower than 10–15 s for the IEA 15-MW rotor. With the unsteady airfoil correction deactivated (*BEM no UA* in Fig. 4(a)), this trend vanishes. Therefore, it can be concluded from the DBEM results that the unsteady airfoil effect is not active in the flat region (plateau) in Fig. 4(a), i.e. at motion periods lower than the one at which the saddle point in Fig. 4(d) occurs. Since the unsteady airfoil correction in OpenFAST DBEM has shown to be reliable in predicting the occurrence of the unsteady airfoil effect in the past, this conclusion reflects the physical behaviour, although it is drawn from the results of a correction method.

The gradual reduction of the thrust force amplitude between 500 s and 70 s is predicted by all three methods in all load case series of the IEA 15-MW rotor and can ultimately not be caused by the unsteady arifoil or returning wake effect. Therefore, the dynamic wake effect seems to cause this reduction since it is the only known unsteady phenomenon impacting the global loads of a wind turbine in a relevant manner. This conclusion is supported by the DBEM results. Another hint on this can be found by comparing the results of the DBEM with (*DBEM*) and without unsteady airfoil correction (*DBEM no UA*) in Fig. 4(a). In this case, the dynamic wake correction is the only source of unsteady behaviour, because the BEM itself is quasi-steady. It is obvious that the gradual reduction from high to intermediate periods is caused by this correction method. This pinpoints that the dynamic wake effect is the source of this behaviour. The same can be argued in case of the IEA 22-MW rotor; however, the effect takes place at higher motion periods (see Fig. 4(d) and (e)). Although the principal impact of the dynamic wake effect is modelled similarly by all methods, the magnitude of the reduction deviates between the results of the FVW methods and the DBEM method. A more detailed investigation of these differences caused by the dynamic wake effect is given in Section 4.4.

In summary, both rotors seem to be impacted by the unsteady phenomena in the same way: The dynamic wake effect causes a gradual reduction of the amplitude from high to intermediate periods. The unsteady airfoil and returning wake effect lead to another decrease of the thrust amplitudes at low motion periods, reaching a minimum when f_p equals unity. Interestingly, the impact of the dynamic wake effect calculated by the FVW methods is much stronger in the case of the IEA 22-MW rotor compared to the IEA 15-MW rotor, which will also be examined in the next sections. In addition, all unsteady effects seem to come into action at slightly higher motion periods in the case of the IEA 22-MW rotor in Fig. 4(d) and (e). This can be detected by the motion period corresponding to the minimum amplitude caused by returning

[13] In contrast to this, a normalised amplitude equalling unity does not necessarily indicate the absence of such effects, as the impact of two effects may compensate each other.

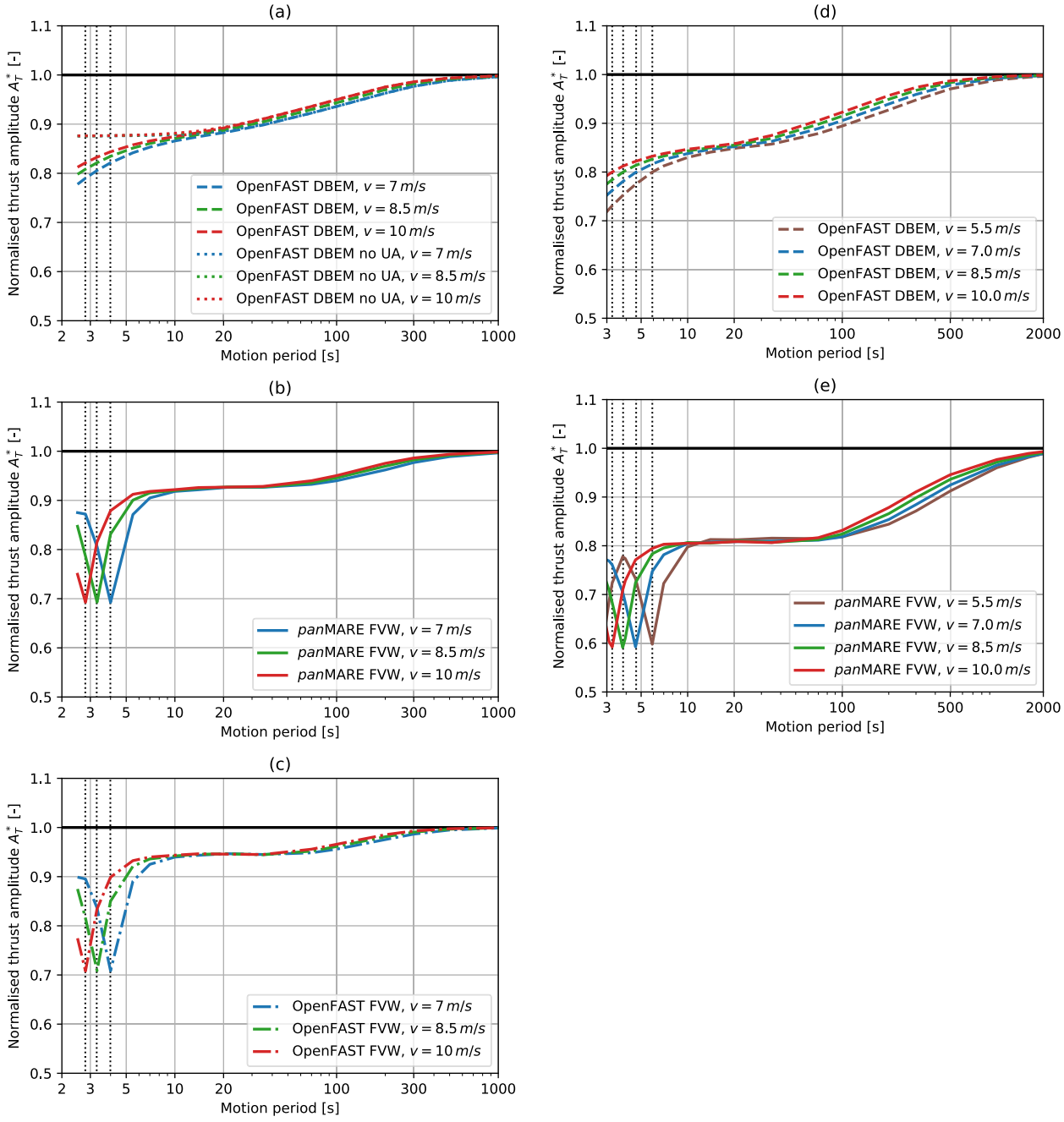

Fig. 4. Normalised rotor thrust force amplitude A_T^* for varying surge motion periods for all wind conditions as defined in Table 2. Results for the IEA 15-MW rotor are shown on the left side (a-c) while graphs on the right are obtained from simulations of the IEA 22-MW rotor (d-e). Results obtained from the same simulation methods are shown in the same row. A logarithmic scale is applied to all x-axes.

wake effect: It moves towards the lower limit of the relevant wave period range (approx. 5 s) at a wind speed of 7 ms^{-1} (Fig. 4(e)). When considering a wind speed of 5.5 ms^{-1}, $f_p = 1$ (i.e. the minimum) lies clearly within the realistic wave/tower top motion periods for the IEA 22-MW rotor. Although this minimum is outside the wave period range at higher wind speeds, a notable impact of the returning wake effect is present in the lower part of the wave period region for nearly all cases. Furthermore, the plateau in Fig. 4 (b, c and e) as well as the saddle point in Fig. 4(a) and (b) indicate that the impact of the dynamic wake effect is fully evolved in the wave period region. As a consequence, the thrust force amplitude of both rotors is clearly impacted by the dynamic wake effect in all realistic motion conditions.

4.3. Generalisation

When comparing the load case series for various wind speeds in Fig. 4 (all graphs), the main difference between the thrust force amplitudes caused by the variation of the wind speed is a shift to lower periods with increasing wind speed. This indicates that the observed behaviour can be generalised by means of the rotor reduced frequency f_r, which includes a normalisation on the wind speed. Figs. 5 and 6 illustrate the same simulation results as shown in Fig. 4 for the IEA 15-MW and the IEA 22-MW turbines. However, the results are plotted over f_r instead of the motion period, and the results of all methods are shown in one graph. The x-axis shows decreasing reduced frequencies from

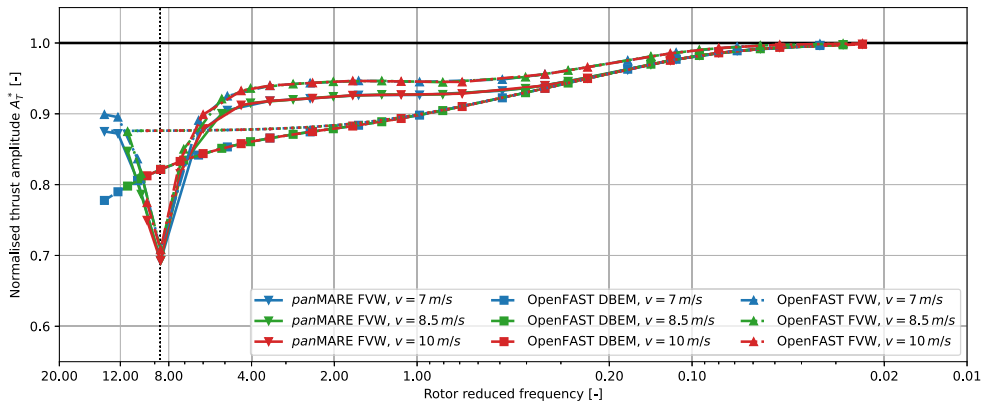

Fig. 5. Normalised rotor thrust force amplitude A_T^* of the IEA 15-MW rotor for the cases shown in Fig. 4 (a-c). Motion periods are expressed in terms of f_r (see Eq. (6)) on the x-axis. The x-axis is displayed reversed and in a logarithmic scale.

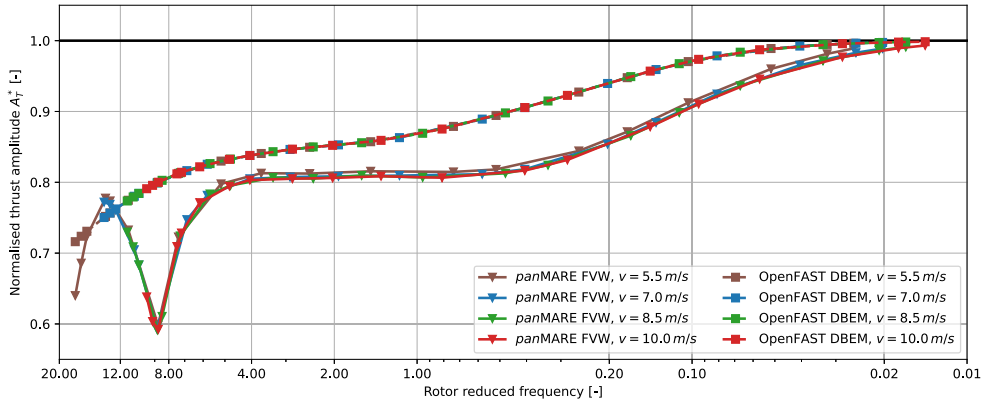

Fig. 6. Normalised rotor thrust force amplitude A_T^* of the IEA 22-MW rotor for the cases shown in Fig. 4 (d-e).

left to right in order to keep the same visual appearance compared to Fig. 4.

As a result of the normalisation of the motion period in terms of f_r, the lines for all three load case series lie exactly on top of each other for the three individual methods in both figures. This can be explained by considering the three dimensionless numbers characterising the three unsteady aerodynamic phenomena (see Section 2) that determine the trend of the thrust force amplitude:

- f_r is the dimensionless number determining the occurrence and strength of the dynamic wake effect. It is therefore straightforward that the strength of the gradual reduction of the thrust amplitude caused by the dynamic wake effect between $f_r \approx 0.05$ and $f_r \approx 0.5$ (for the FVW methods) is the same for all wind conditions at a given f_r.
- The airfoil reduced frequency f_a determines the strength of the unsteady airfoil effect and influences the occurrence of the returning wake effect. It is defined by the ratio of motion frequency and the local blade inflow velocity for a given radius. When rewriting Eq. (5) for the airfoil reduced frequency in terms of the TSR (λ), it becomes clear that it is proportional to the rotor reduced frequency for a certain rotor at constant TSR:

$$f_a(r) = \frac{f}{v_0}\frac{\pi c(r)}{\sqrt{1+\left(\frac{r}{R}\lambda\right)^2}} = \frac{f_r}{2R}\frac{\pi c(r)}{\sqrt{1+\left(\frac{r}{R}\lambda\right)^2}} \tag{11}$$

$$f_a \propto f_r \text{ for } \lambda, \text{c(r)}, \text{r and R const.} \tag{12}$$

Therefore, the distribution of f_a over the blade is linearly dependent on f_r.[14] Consequently, an identical f_r results in the same distribution of f_a over the blade ultimately causing the same impact of the unsteady airfoil effect in Figs. 5 and 6. This identical behaviour becomes apparent when comparing the DBEM simulations at high reduced frequencies for the three wind velocities.

- The motion to blade passing frequency ratio f_p characterises the impact of the returning wake effect on the thrust force amplitude in combination with f_a. Analogous to the airfoil reduced frequency, it can be shown that f_p is linearly dependent on f_r:

$$f_p = \frac{f}{v_0}\frac{2\pi R}{n_b \lambda} = f_r \frac{\pi}{n_b \lambda} \tag{13}$$

$$f_p \propto f_r \text{ for } \lambda \text{ const.} \tag{14}$$

Consequently, $f_p = 1$ is reached at the same rotor reduced frequency for all considered wind speeds in Figs. 5 and 6, provided that the TSR is constant. This leads to the observed behaviour, where the minimum caused by the returning wake effect occurs at the same f_r in every load case series for the individual turbines.

As the three relevant dimensionless numbers vary linearly with each other, the unsteady behaviour of one specific rotor can be characterised by the reduced frequency at constant TSR.[15] The fact that all wind conditions lead to a nearly identical behaviour of the unsteady thrust

[14] provided that the same rotor and TSR are considered.

[15] The above derivation does not include a variation of the motion to inflow velocity ratio. However, it is shown later in the text that the conclusion holds true for all moderate motion to inflow velocity ratios.

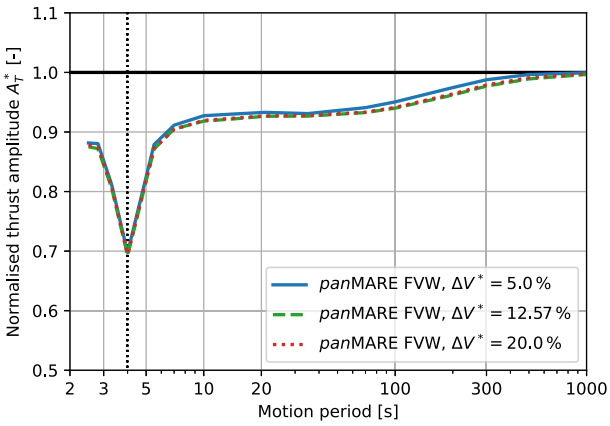

Fig. 7. Normalised rotor thrust force amplitude A_T^* for varying surge motion periods for the 7 ms^{-1} wind condition with varied motion velocity amplitudes.

force amplitude when plotting them over f_r in Figs. 5 and 6 is therefore in line with theoretical expectations.

Rule of thumb to predict the returning wake effect

Another useful relation can be found when expressing f_p in terms of the rotor reduced frequency as shown in Eq. (13). As the first minimum of the thrust force amplitude occurs at $f_p = 1$, a rule of thumb can be given for a three-bladed rotor to estimate the corresponding rotor reduced frequency:

$$f_p = f_r \frac{\pi}{n_b \lambda} = 1 \Rightarrow f_r = \lambda \frac{n_b}{\pi} = \lambda \frac{3}{\pi} \approx \lambda \tag{15}$$

The minimum of the rotor thrust force amplitude therefore occurs approximately when the rotor reduced frequency approaches the TSR. This rule of thumb can be applied to any modern three-bladed wind turbine, because these reach similar levels of f_a in operation, which is the second prerequisite of the occurrence of the returning wake effect.

Variation of ΔV^*

The findings from the analysis of the simulation results can be directly transferred to other surge velocity amplitudes ΔV^*. As shown for the IEA 15-MW rotor at a wind speed of 7 ms^{-1} in Fig. 7, the behaviour of the thrust force amplitude is insensitive to variations of ΔV^* (at least in a moderate range). This can be understood by considering the impacts of the unsteady airfoil effect and the returning wake effect: Both can be considered as perturbations of the quasi-steady lift force amplitude (see [26]). The unsteady lift force A_L (i.e. the variation of the sectional thrust force) can therefore be expressed as a function of the quasi-steady lift force amplitude $A_{L,qs}$ and a perturbation function $P(f_a, f_p)$ for a given f_a and f_p:

$$A_L = A_{L,qs}\, P(f_a, f_p) \tag{16}$$

where $P(f_a, f_p)$ contains the combined impact of the unsteady airfoil and returning wake effect on airfoil level. Therefore, the unsteady contributions from these effects scale with the quasi-steady amplitude $A_{T,qs}$ no matter how strong it is altered by variations of ΔV^*. This observation also seems to apply for the impact of the dynamic wake effect, which is further investigated in Section 4.4.

Four phases of the response

The fundamental behaviour of the thrust force response generated by harmonic tower top surge motions for the two turbines considered can be characterised as shown in Fig. 8. The sketch shows four phases (from high to low motion periods): In phase I, the thrust force amplitude equals the quasi-steady one and stays constant for $f_r \ll 0.05$ (no unsteady contribution). In phase II, the dynamic wake effect starts affecting the amplitude, and the amplitude decreases as the frequency increases. The onset of this decrease is observed between $f_r \approx 0.02$ and $f_r \approx 0.05$ for the different rotors in the FVW methods. Third, a plateau is reached (dynamic wake effect fully evolved). In the case of the FVW simulations, the plateau is reached at $f_r \approx 0.5$. However, this limit is predicted differently by the DBEM method. The level of the plateau ($\Delta A^*_{\mathrm{T,dyn.\ wake}}$) is predicted differently by the methods and seems to be turbine-dependent. In phase IV, the unsteady airfoil and the returning wake effect start to further decrease the amplitudes with higher f_r. In this phase, all three unsteady phenomena impact the thrust force amplitude. While a minimum is caused by the returning wake effect at $f_p = 1$, i.e. $f_r \approx \lambda$, it is assumed that the effect starts to impact the thrust force amplitude from $f_p > 1/4$, i.e. $f_r > \lambda/4$. The unsteady airfoil and returning wake effect need to be considered together since the impact of the latter can be thought of as a perturbation on the decrease of the lift force caused by the former effect. Therefore, the returning wake effect cannot occur, when the limiting condition for the unsteady airfoil effect ($f_a > 0.02$) is not given. In contrast to this, the unsteady airfoil effect may occur in isolation when $f_p < 1/4$ and $f_a > 0.02$. It is important to note again that f_a is an airfoil-related dimensionless number, which varies over the blade span. Therefore, $f_a > 0.02$ must be true for a considerable portion of the blade in order to trigger a notable impact of the unsteady airfoil (and returning wake) effect on the rotor thrust. For even lower motion periods, an oscillation of the thrust force amplitude seems to happen. Minima occur when the motion frequency is an integer multiple of the blade passing frequency, i.e. $f_p = m$ and maxima at $f_p = (2m + 1)/2$.[16] For the two turbines considered, the first minimum is approximatively 20% less than the value in phase III ($\Delta A^*_{T,ret.wake}$).

Context with previous works

The characteristic behaviour of the thrust force amplitude investigated in previous works can also be described in terms of the four phases shown in Fig. 8. However, some aspects seem to depend on the rotor and its modelling. Phase II reaches different values when the dynamic wake effect is fully evolved (plateau level, phase III) for the IEA 15-MW and the IEA 22-MW rotors in the case of the FVW simulations.[17] The same is true when comparing the FVW results against AeroDyn's results. For other rotors, this distance between the plateau level and the quasi-steady amplitude ($\Delta A^*_{\mathrm{T,dyn.\ wake}}$) may also tend to zero (e.g. the UNAFLOW and the TUHH rotors in [3,4,9,12]) or a slight increase can occur ($\Delta A^*_{\mathrm{T,dyn.\ wake}} < 0$). Such behaviour was observed for the Vestas V90 in [10]. In these cases, phases I,II and III cannot be distinguished when considering the behaviour of the thrust amplitude only. This is most likely the reason why the above characterisation of the unsteady behaviour of the thrust force amplitude has not been performed in such detail in previous studies. The reason for these different behaviours is investigated in the next section.

For the UNAFLOW and the TUHH model rotors, a slight increase of the thrust force amplitude occurs at the motion frequency, which equals half the blade passing frequency ($f_p = 0.5$). This is most likely a consequence of the returning wake effect (see [3]). However, such characteristic is not present for the considered large-scale turbines. This behaviour is still a matter of investigation.

The drop of the thrust force amplitude from the plateau to the minimum ($\Delta A^*_{\mathrm{T,ret.\ wake}}$) caused by the returning wake effect is a bit

[16] Where m is an integer starting from 1.

[17] When comparing *pan*MARE's present results for the IEA 15-MW rotor with those shown in [3], the evolution of the plateau is predicted on a lower level, although the same rotor model is used. This is due to the fact that the quasi-steady amplitude $A_{T,qs}$, used to normalise the unsteady amplitudes, was chosen to be the result of the simulation with the maximum motion period of 300 s. In contrast to this, the definition in Eq. (8) is used in the present work. Therefore, the reference amplitude for the IEA 15-MW rotor in [3] is slightly wrong.

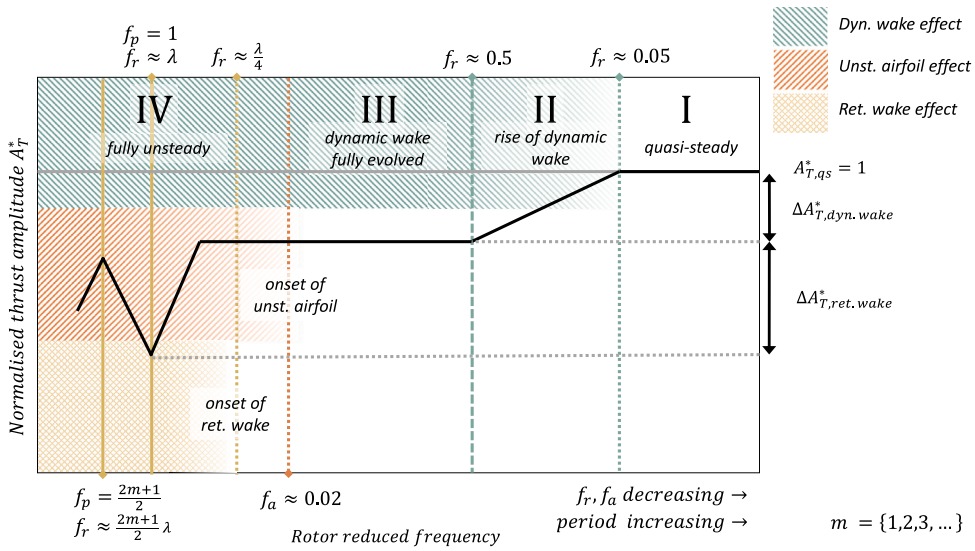

Fig. 8. Sketch of the overall behaviour of the normalised rotor thrust force amplitude A^*_T for constant surge velocity amplitudes and varying motion periods. Limits between the phases in terms of f_r are approximate values derived from the FVW simulations.

more than 20% for the large-scale rotors. In contrast to this, the model rotors show a drop of approximately 30%. This might be caused by the consistently higher level of f_a at the blade sections of the experimental rotors, which indicate a stronger vortex shedding. The higher level of f_a is a consequence of the specialised design of the model rotors reaching high Reynolds numbers at the blades. However, a proof for this correlation is not given in this work.

Comment on universal validity

When combining the findings of the present numerical study and the previous studies mentioned above, a first impression on the universal validity of the proposed generalised characteristic can be derived. The derivation of the four phases of response is physics-based and therefore independent from the considered rotor. It can be expected that the given f_r for the transition between phases I, II and III will hold for any typical wind turbine rotor. This is due to the fact that the occurrence of the dynamic wake effect is known to be independent from the rotor design, but determined by rotor size, inflow velocity and frequency of external forcing (i.e. f_r, see Section 2). However, for different turbines and operating conditions, the borders between phase III and IV may be shifted significantly. For example, a lower TSR would shift the onset of the returning wake effect to lower f_r so that phase III may cover a significantly smaller period range. This can be easily predicted by the dimensionless numbers shown in Fig. 8. In contrast to this, the change of the thrust amplitude from phase I to phase III ($\Delta A^*_{\mathrm{T,dyn.\ wake}}$) or from phase III to the minimum in phase IV ($\Delta A^*_{T,ret.wake}$) is most likely dependent on the rotor design and -TSR. These values will therefore have to be computed by a similar study as performed in this work for one moderate ΔV^* and can then be applied to any moderate surge motions (see Section 5).

4.4. Induced velocities and dynamic wake effect

The fact that the unsteady airfoil and returning wake effect cannot be active in phase II in Fig. 8 since $f_a \ll 0.02$ already gives indication that the dynamic wake effect causes the gradual reduction of the thrust force amplitude in this phase. However, a better understanding of the impact of this effect on the rotor loads can be obtained by investigating the change of the axial induced velocity in this range of motion periods. Unfortunately, the definition of the axial *induced velocity* (and axial induction) is often different in BEM and FVW methods. In the following comparison, the rotor averaged axial induced velocity is used to compare the results of the different methods in order to exclude the impact of trailing vorticity from the results of the FVW method. A more detailed explanation for this choice and how the induced velocity is computed is given in Appendix C. The load case series with 7 ms^{-1} wind speed and the IEA 15-MW rotor are chosen as the subject of investigation.

Fig. 9 shows the rotor averaged axial induced velocity calculated by OpenFAST DBEM and *pan*MARE for selected motion periods. The induced velocity is normalised by the wind speed. The dashed grey lines indicate steady simulations with an inflow velocity of v_0+V_m and v_0-V_m representing the quasi-steady behaviour at the maximum and minimum relative inflow velocities. For the case where the period is 1000 s, the axial induced velocity exactly reaches the theoretical minimum and maximum values. However, the normalised quasi-steady peak-to-peak amplitude $\Delta v^*_{ind,qs}$ is nearly 40% lower in *pan*MARE compared to OpenFAST DBEM. With decreasing motion period, both methods predict an attenuation of the amplitudes to nearly zero at the lowest motion periods. In addition, a significantly rising phase shift develops with decreasing period, which is slightly stronger in case of *pan*MARE. This behaviour is generally in line with the expected impact of the dynamic wake effect. We note that even at the extremely large motion period of 1000 s the maximum does not occur exactly at a motion phase of 0°. This indicates that a small contribution of the dynamic wake effect is present in this case.

In order to obtain a direct comparison between the attenuation characteristics of the methods, the peak-to-peak amplitude of the induced velocity $\Delta v^*_{\mathrm{ind}}$ is normalised to the quasi-steady one[18] and is displayed for all motion periods in Fig. 10. The same motion period scale in Fig. 4 is applied. Overall, the same attenuation trend can be observed for both methods. However, *pan*MARE predicts a stronger attenuation at low and intermediate periods. It seems that the attenuation rate becomes similar for motion periods below 35 s. Yet, the results of *pan*MARE become scattered in this region. This is due to the fact that the calculation of the axial induced velocity based on the instantaneous flow field in *pan*MARE is unable to resolve such low amplitudes accurately.

As the dynamic wake effect theoretically acts like a first-order low-pass filter, the same amplitudes are plotted in the fashion of a Bode plot in Fig. 10(b). The attenuation characteristic of OpenFAST DBEM is

[18] The quasi-steady peak-to-peak amplitude $\Delta v^*_{ind,qs}$ is defined as the difference between the induced velocities at the inflow velocities v_0+V_m and v_0-V_m, i.e. the dashed grey lines in Fig. 9.

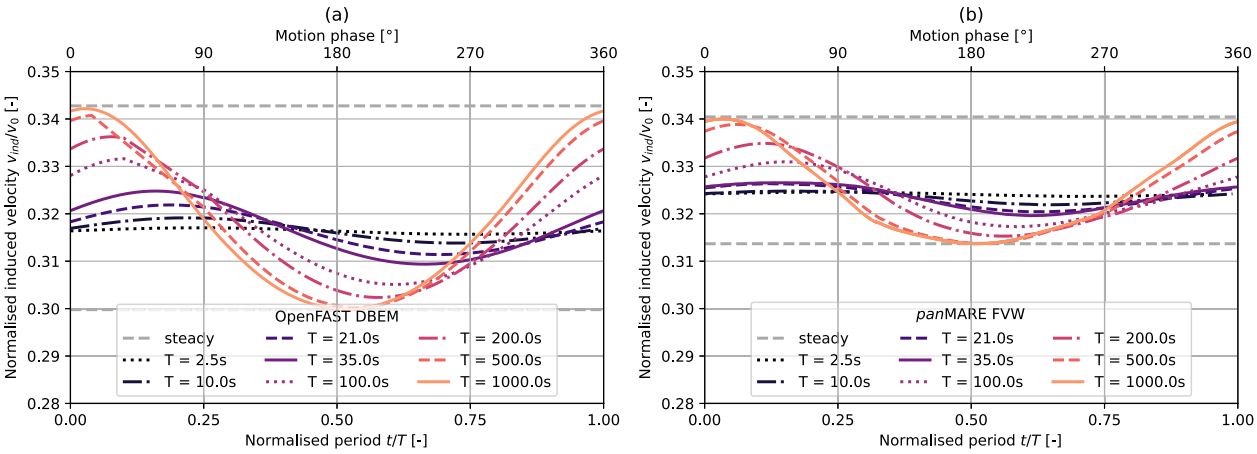

Fig. 9. Illustration of the normalised rotor averaged axial induced velocity of the IEA 15-MW rotor undergoing selected surge motions from the 7 ms^{-1} wind condition in Table 2. Results are obtained by OpenFAST DBEM (a) and *pan*MARE FVW (b) simulations. Dashed grey lines indicate steady results at minimum and maximum relative inflow velocity.

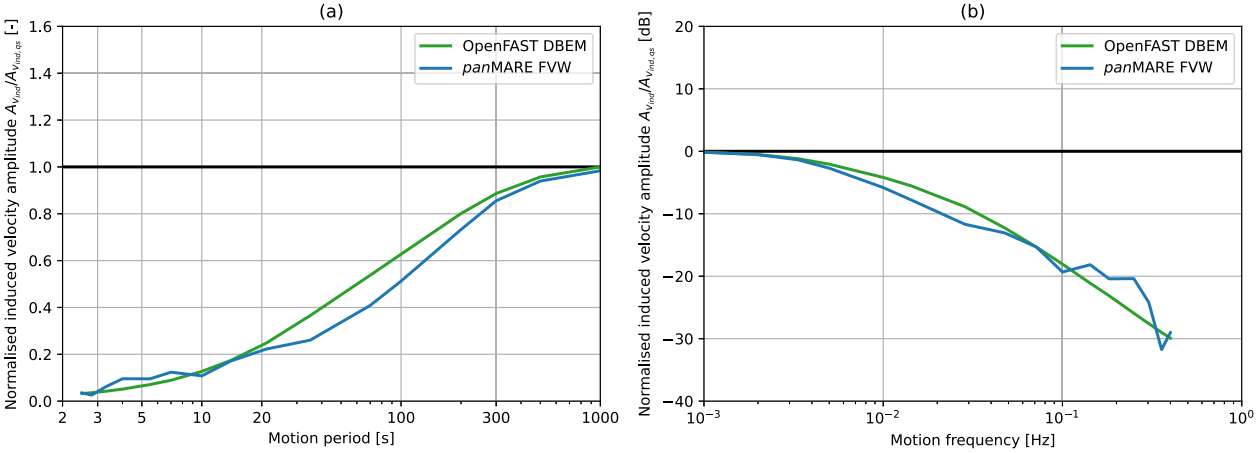

Fig. 10. Normalised amplitudes of the rotor averaged axial induced velocity shown in Fig. 9. (a) x- and y-axes scaled comparable to Fig. 4; (b) Alternative visualisation as Bode plot.

observed to follow a slope of 20 dB per decade for high motion frequencies, which is representative for the behaviour of first-order low-pass filter. For higher motion frequencies, the scattering of the *pan*MARE results prevents further analysis. These findings clearly link the gradual reduction of the thrust force amplitude in phase II to the impact of the dynamic wake effect, since the induced velocity is damped significantly in the corresponding period range. In addition, the methods predict a vanishing fluctuation of the axial induced velocity near the onset of the plateau, which indicates that the dynamic wake effect is fully active but does not change its impact when motion periods decrease. The comparison also shows that the dynamic inflow correction in OpenFAST DBEM is generally able to reproduce the unsteady impact of the dynamic wake effect in this case. However, the attenuation appears too weak compared to the higher fidelity model used here (FVW).

In spite of a fair agreement in the estimation of the attenuation, the methods predict a different level of the plateau (phase III). This, in turn, cannot be attributed to the unsteady modelling of the dynamic wake effect.

Influence of steady behaviour on unsteady thrust force characteristic

Since the level of the plateau reached in phase III (i.e. $\Delta A^*_{\mathrm{T,dyn.\ wake}}$) is not determined by unsteady phenomena itself, it can be concluded that the steady aerodynamic behaviour (and/or modelling) of the rotor plays a major role in this context. In light of the observation that this level can be very different (e.g. at the same height as the quasi-steady response in case of the TUHH and to UNAFLOW rotors), it seems beneficial to investigate the quasi-steady behaviour of the axial induced velocity during an infinitely slow surge motion. The (nearly) quasi-steady case with a motion period of 1000 s in Fig. 9 serves as a starting point for the analysis: At 0 ° motion phase, the rotor is in backward motion and the minimum relative inflow velocity ($v_{\mathrm{in}} = v_0 - V_m$) and minimum thrust force occur (see Fig. 2). The minimum surge position is reached at 90 ° ($v_{in} = v_0$) and the maximum relative inflow velocity during the forward motion occurs at 180 ° ($v_{\mathrm{in}} = v_0 + V_m$). Knowing this, it is remarkable that the induced velocity has a phase shift of 180 ° compared to the relative inflow velocity. At the highest relative inflow velocity (180 °), the lowest induced velocity occurs in Fig. 9. When assuming a similar operational state (i.e. momentum equilibrium), a higher inflow velocity should yield a higher induced velocity to reach a similar axial induction a. This does not seem to be the case, which is a strong hint that the operational state (characterised by the TSR) significantly changes within the quasi-steady motion cycle.

When taking into account this information on the induced velocity, qualitative velocity triangles describing the flow at a representative blade section during one motion cycle can be sketched. The upper row in Fig. 11 shows the velocity triangles for different inflow velocities and a constant rotational speed representing the flow situations at the motion phases 0 °, 90 ° and 180 ° for the limiting case of an infinitely large motion period (no unsteady contributions). While the wind speed v_0 is constant, the relative inflow velocity v_{in} varies between the motion

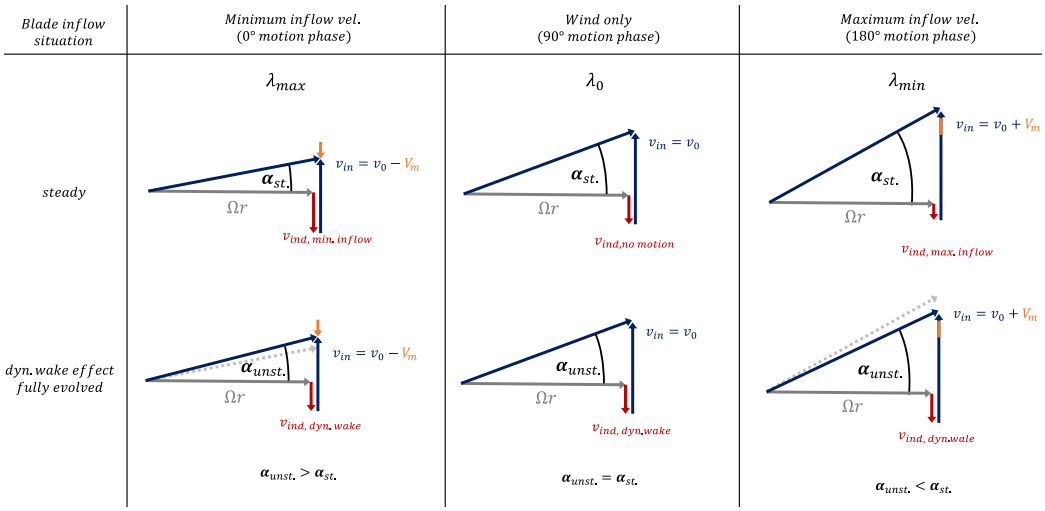

Fig. 11. Simplified sketch of the inflow conditions at a representative blade section of the IEA 15-MW rotor in surge motion. Backward motion, rest position and forward motion conditions are shown from left to right. The upper row represents steady behaviour; the lower row includes the impact of the dynamic wake effect. The blade twist angle is disregarded for the sake of simplicity. For comparison, the steady inflow vector is shown in the unsteady situation with dotted grey lines.

phases, which results in a variation of the TSR. The axial induced velocity is maximum for the minimum relative inflow velocity and the other way around as it can be read from Fig. 9.

The second row of Fig. 11 shows the unsteady situation, where the dynamic wake effect is active and damps the induced velocity variation towards zero (phase III). For the sake of simplicity, it is assumed that no influence of the unsteady airfoil or returning wake effect is present in this case. The dynamic wake effect causes a constant induced velocity $v_{\text{ind, dyn. wake}}$ for all motion phases (see second row of Fig. 11) since the variation is damped completely. All other velocities remain unchanged in comparison to the upper row. In the case of the backward motion (0 °), the impact of the dynamic wake effect leads to a higher angle of attack compared to the steady case, because the induced velocity decreased from the steady to the unsteady case. The opposite happens in case of the forward motion (180 °). As a consequence, the thrust force increases at 0 ° motion phase (backward motion) and decreases 180 ° (forward motion) compared to the quasi-steady case, which is equivalent to the behaviour discussed in the previous sections: an increase of the thrust force minimum and a reduction of the thrust force maximum during the surge motion cycle. This yields a decrease of the amplitude to a constant level (plateau) in case the dynamic wake effect has fully evolved, while no other unsteady effects come into play. Knowing this, it is clear that the impact of the dynamic wake effect on the thrust force amplitude increases with the magnitude of change of the induced velocity between 0 ° and 180 °. The sensitivity of the axial induced velocity on changes of the inflow wind speed therefore determines how strong and in which direction the thrust force amplitude is altered due to the dynamic wake effect.[19]

Influence of turbine design and modelling on dynamic wake effect

The sensitivity of the axial induced velocity on changes of the inflow velocity is dependent on rotor and modelling approach. This sensitivity is closely linked to the a-TSR curve shown in Fig. 12, where the axial induction a is shown over a varying TSR. The figure is derived from steady *pan*MARE simulations, in which the inflow velocity is varied while the rotational speed is kept constant so that the quasi-steady flow situations at 0 ° and 180 ° motion phase are covered (marked with dashed vertical lines). The diverging trend of inflow velocity and axial induction is clearly visible in the figure: The axial induction (blue line)

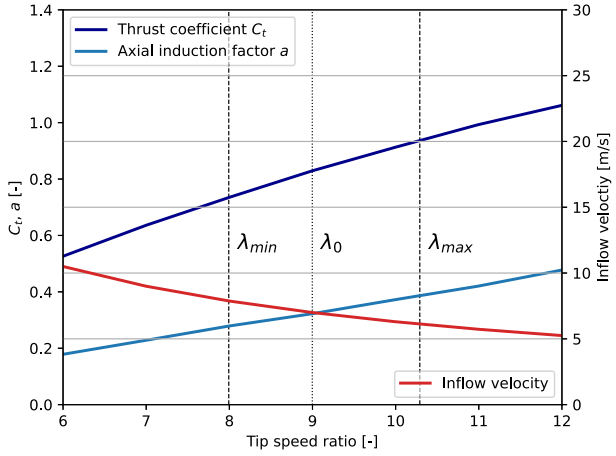

Fig. 12. Thrust coefficient, axial induction and inflow speed of the IEA 15-MW rotor at constant rotational speed over TSR. Results are obtained from steady *pan*MARE simulations with uniform winds and no tower top motion. The nominal operation condition at optimum TSR is indicated by the vertical dotted line. The dashed lines mark the TSR reached at minimum and maximum inflow velocity adapted from the load case series with 7 ms^{-1} wind speed in Table 2.

increases with decreasing inflow velocity (red line) and increasing TSR at constant rotational speed. The axial induced velocity is simply the product of axial induction and inflow velocity and is shown in Fig. 13. All shown quantities, except the TSR, are normalised to their value at $v_{\text{in}} = v_0$ (no motion) in this Figure. The induced velocity is maximum, when v_{in} is minimum (maximum backward motion velocity) at λ_{max} and the other way around, which reflects the behaviour of the steady velocity triangles. Finally, the amplitude of the axial induced velocity $\Delta v^*_{ind,qs}$ during a quasi-steady surge motion cycle can be read from the difference of the axial induced velocities at $\lambda_{\text{min}}(\Omega, v_{\text{in,max}})$ and $\lambda_{\text{max}}(\Omega, v_{\text{in,min}})$. This difference exactly equals the difference between the dashed lines in Fig. 9. $\Delta v^*_{ind,qs}$ determines the impact of the fully evolved dynamic wake effect on the thrust force amplitude, which defines the level of the plateau in phase III in Fig. 8.

The reduction of the thrust force amplitude by the fully evolved dynamic wake effect is the same for different surge motion velocity

[19] This applies for a constant rotational speed.

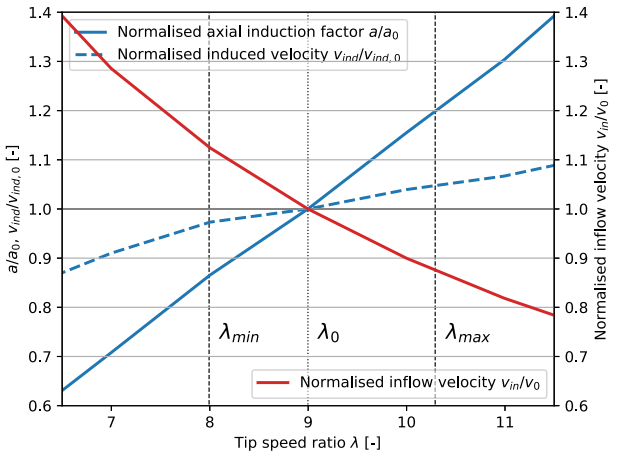

Fig. 13. Same data as shown in Fig. 12 but without thrust coefficient. A dashed line representing the induced velocity is added. All quantities are normalised to their value at nominal operating conditions (i.e. a wind speed of 7 ms^{-1} and no tower top motion).

amplitudes ΔV^* (see Fig. 7). This is due to the fact that both the quasi-steady thrust force amplitude $A_{T,qs}$ and the quasi-steady amplitude of the induced velocity $\Delta v^*_{\mathrm{ind,qs}}$ show a linear dependency on the motion velocity amplitude ΔV^*.[20] In both cases, this linear dependency can be assumed for moderate values of ΔV^*, while this trend may change in case of extreme motion conditions.

The influence of the dynamic wake effect on the normalised thrust force amplitude A^*_T for moderate ΔV^* can therefore be determined by the steepness of the induced velocity with regard to the TSR. A high steepness indicates a strong influence of the dynamic wake effect on the angle of attack and ultimately on the normalised thrust force, resulting in a high $\Delta A^*_{\mathrm{T,\ dyn.\ wake}}$ (plateau level, see Fig. 8).

In order to gain a valid comparison of this steepness for different rotors, the x-axis in Fig. 13 can be normalised to the nominal TSR in no-motion conditions. In Fig. 14 (a-c) the resulting graphs are shown for the IEA 15-MW, IEA 22-MW and the UNAFLOW rotors. The results are obtained by OpenFAST DBEM and *pan*MARE. In contrast to Fig. 13, only two points at the corresponding nominal, minimum and maximum inflow velocities are directly calculated while the trend is visualised by a linear fit. For the IEA 15-MW rotor, OpenFAST DBEM shows a larger steepness than *pan*MARE, while the opposite is the case for the 22-MW rotor. The qualitative ratio of the steepness in the different cases compares well to the plateau levels reached in Figs. 5 and 6.[21] In case of the UNAFLOW rotor, the steepness is significantly smaller, resulting in a nearly vanishing $\Delta A^*_{\mathrm{T,\ dyn.\ wake}}$. This is in line with the aforementioned observations from different simulation studies, where no impact of the dynamic wake effect on the thrust force amplitude was found.

Finally, it seems evident that the impact of the fully evolved dynamic wake effect can be determined by the steepness of the normalised axial induced velocity over the tip speed ratio $\frac{dv^*_{\mathrm{ind}}}{d\lambda}$ at constant rotational speed. Positive values indicate that the level of the plateau lies below the quasi-steady amplitude, while negative values should result in a higher level of the plateau. Typically, a larger steepness results in a larger impact of the dynamic wake effect on the thrust force amplitude. Due to the fact that the steepness does not directly express the influence of TSR changes on the thrust force but on the angle of attack, the comparison between different rotors may contain slight deviations in terms of the thrust force amplitude.

It has to be noted that the above analysis is based on two different ways of exporting the axial induced velocity in the two methods, which might cause some deviations. However, the authors expect that the trend of the induced velocity is not significantly altered by this fact.

Context with previous works

Papi et al. [9] also offered an explanation for the fact that the dynamic wake effect impacts the induced velocity but not the rotor thrust force amplitude of the UNAFLOW rotor: The authors show, by means of a simulation study, that the induced velocity is in phase with the relative inflow velocity at the inner blade parts while it is 180° shifted at the outer blade parts. Consequently, the dynamic wake effect has an opposite effect on the inner and the outer blade parts. Papi et al. [9] therefore argue that the impact of the dynamic wake effect cancels out between the inner and the outer blade parts. These findings are in line with the current simulations. However, the 180° phase shift of the induced velocity is not unique for the UNAFLOW rotor. It is a consequence of the fact that the sensitivity of the angle of attack (and rotor loading) to changes of the wind speed is very different in the inner and outer blade parts. This generally applies for typical wind turbine rotors. The unique characteristic of the UNAFLOW rotor seems to be the following: The two blade regions where the induced velocity has a phase shift of 0° and 180° with regard to the relative inflow velocity are distributed in a way that their contributions to the overall induced velocity fluctuation cancel out. Therefore, the overall (rotor averaged) amplitude of the induced velocity tends to zero in the quasi-steady case. As the dynamic wake effect only acts on this tiny variation, no distinct impact develops on the thrust force. In the case of the IEA 15-MW and 22-MW rotors, such phase shift is also present. However, for these rotors, the two blade regions do not cancel out exactly so that a relevant influence of the dynamic wake effect on the thrust force amplitude is present.

It was found in the previous sections that the axial induced velocity fluctuation caused by the surge motion is damped by the dynamic wake effect. At very low motion periods, the amplitude of the fluctuation tends to zero, which is in line with theoretical expectations. This is also in accordance with the findings of Papi et al. [9] showing that the dynamic inflow correction damps the induced velocity. The fact that Sanvito et al. [12] found increasing fluctuations of the axial induction with lower periods can be explained by the different definitions of the axial induced velocity.[22] While the axial induced velocity in [12] contains contributions from trailing and shed vorticity, the present study and common DBEM methods only consider the contribution of the trailing vorticity as induced velocity (see Appendix C). The unsteady airfoil and the returning wake effect therefore cause strong changes of the induced velocity calculated by Sanvito et al. at low motion periods in phase IV (see Fig. 8). These are naturally not damped by the dynamic wake effect.

5. Impact of unsteady effects in realistic environmental conditions

In order to demonstrate the relevance of the identified unsteady phenomena for large-scale FOWT, their impact is shown in a simple scenario. In this scenario, a 22 MW semi-submersible FOWT is subjected to realistic wind and wave conditions, and the unsteady contribution to the fluctuation of the rotor thrust force is evaluated. The semi-submersible is an upscaled version of the VolturnUS-S platform equipped with the IEA 22-MW as described in [28]. Fully coupled simulations are performed using OpenFAST, and the corresponding

[20] The linear dependency of the quasi-steady thrust force amplitude on ΔV^* has been observed for a number of turbines in a moderate range of ΔV^* (e.g. [3] or [27]).

[21] This applies for method-to-method and rotor-to-rotor comparisons.

[22] Sanvito et al. [12] use the *absolute axial induction*, which is linearly dependent on the axial induced velocity in the absolute reference frame used in this work.

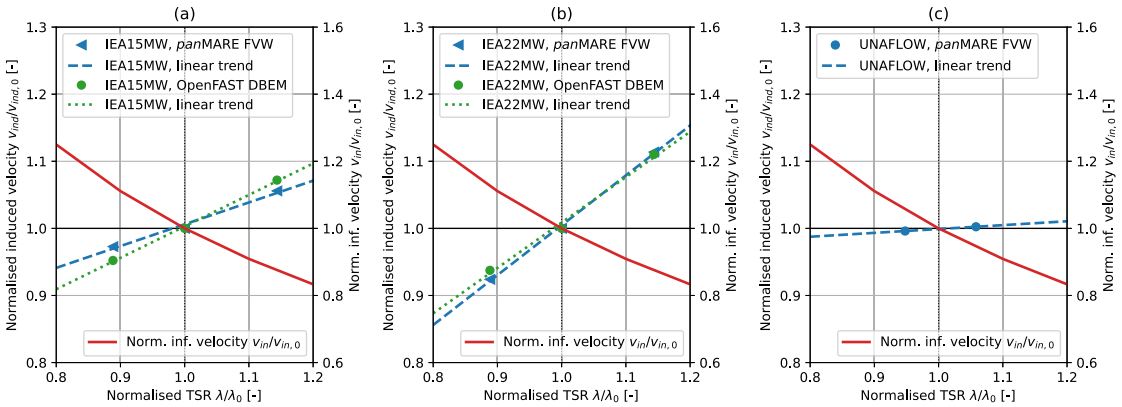

Fig. 14. Comparison of the normalised axial induced velocity over TSR for the IEA 15-MW (a), IEA 22-MW (b) and UNAFLOW (c) rotors computed with OpenFAST DBEM and *pan*MARE FVW. Data points illustrate the values at wind speed as well as minimum and maximum inflow velocity adapted from moderate surge motions. Dashed lines show a linear fit based on the data points. The TSR is normalised by its nominal value at below-rated wind conditions for the individual turbines.

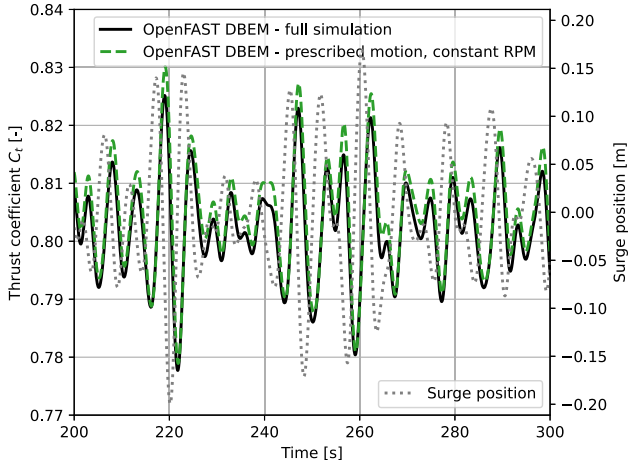

Fig. 15. Exemplary thrust coefficient fluctuations of a 22-MW semi-submersible FOWT in irregular waves with $H_s = 1.5$ m and $T_p = 6.5$ s at a uniform wind speed of 5.5 ms^{-1} computed with OpenFAST (black) compared to a simplified simulation with prescribed tower top surge motion and constant rotational speed.

FOWT model available at the official repository.[23] In order to maintain a clear identification of unsteady phenomena, the blades are assumed to be rigid. For the same reason, wind turbulence, wind shear and the influence of the tower on the flow field are excluded from the analysis. The pre-twisted blade geometry described in Appendix B is utilised. Apart from these simplifications, the full model including active turbine control and tower flexibility is used.

The semi-submersible is subjected to a randomly generated wave time series based on a JONSWAP spectrum with $H_s = 1.5$ m and $T_p = 6.5$ s as well as uniform wind with a speed of 5.5 ms^{-1}. This choice represents a frequently occurring wind and wave condition for the calm and medium sites Gran Canaria Island and Gulf of Maine, but can also be considered as typical for the harsh West of Barra site, which were investigated in [29,30]. In order to further simplify the demonstration case, it is assumed that the motion induced thrust force fluctuations are mainly caused by the tower top surge motion and rotor speed variations are very small. Therefore, the tower top motion trajectory in surge direction is extracted from the coupled simulations and fed into a pure aerodynamic simulation with a constant rotational speed. The rotational speed of 3.48 rpm represents the average value of the fully coupled simulation. Fig. 15 shows a comparison of the thrust force calculated by the fully coupled (black) and the simplified (green) simulations. From the good agreement of the full and the simplified simulations it can be concluded that the thrust force fluctuations are dominated by the tower top surge motion velocity as it is argued in Section 2.3.

Fig. 16 shows the thrust force response for the simplified scenario calculated with OpenFAST DBEM (green) and *pan*MARE (blue). The actual thrust force is normalised to its mean value for the individual methods. In addition, a quasi-steady reference is shown in grey for both simulations. While the unsteady corrections are simply turned off in OpenFAST BEM to obtain this reference, this cannot be done in a FVW method. In *pan*MARE, the reference is created by extracting the actual relative inflow velocity and TSR every time step and calculating the thrust force from a lookup table. The table contains steady simulation results for the corresponding inflow velocities and TSRs. Both methods predict a significant decrease of the thrust force fluctuation compared to their steady reference. When considering the average peak-to-peak amplitude, the unsteady aerodynamic effects lead to a reduction of 21% in the case of OpenFAST DBEM and 30% in case of *pan*MARE compared to the quasi-steady cases. The reduction is considerable in both cases. However, it is comparable to the reduction of the thrust force amplitude in the harmonic surge motion cases in Fig. 4: Here, OpenFAST DBEM predicts a reduction of approximately 19% while a reduction of 35% can be read from *pan*MARE's results at a motion period of 6.5 s and a wind speed of 5.5 ms^{-1}. This is in line with the reduction of the thrust force amplitude shown in the generalised thrust characteristic in Fig. 6 at the corresponding rotor reduced frequency calculated by means of wind speed and wave period. Therefore, it seems that the characteristic of the thrust force amplitude in Fig. 6 can serve as a transfer function from the quasi-steady to unsteady thrust force response. The deviation between the reduction rates in the realistic (this section) and the idealised (Section 4.3) case in *pan*MARE is due to the fact that the reduction is very sensitive to small deviations in the motion period in this region. The tower top period is not constant in the irregular sea state, therefore the reduction from the transfer function is not met exactly. The strong difference between the reduction predicted by the DBEM and the FVW methods again arises from the occurrence of the returning wake effect that is not modelled in OpenFAST DBEM.

6. Summary and conclusions

The unsteady thrust force response of two large-scale wind turbines to tower top surge motions was investigated with different numerical methods. Two lifting line FVW methods, *pan*MARE and OpenFAST (OLAF), as well as the widely used DBEM method of OpenFAST were

[23] https://github.com/IEAWindSystems/IEA-22-280-RWT

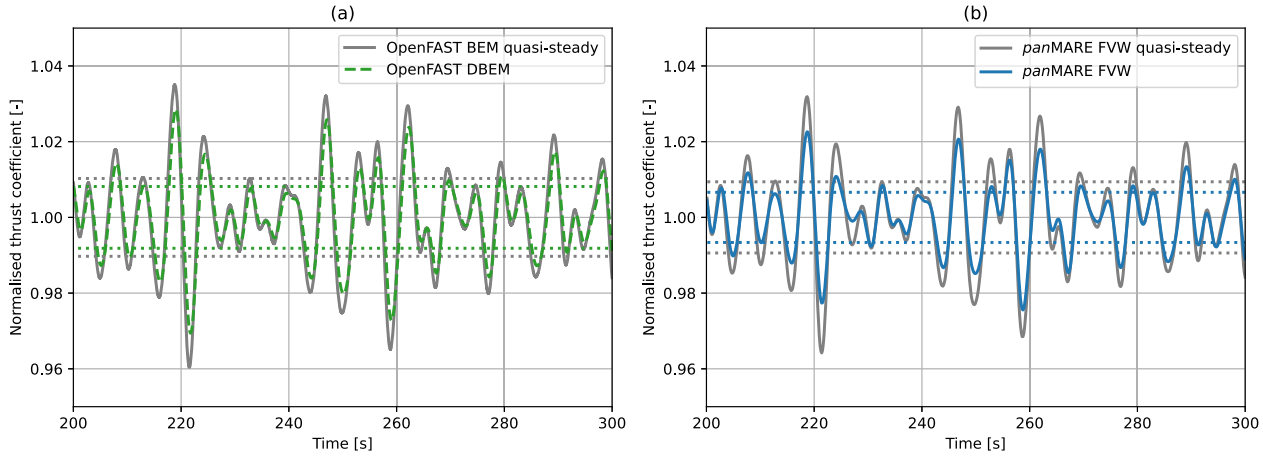

Fig. 16. Normalised thrust force fluctuations of the simplified scenario shown in Fig. 15. OpenFAST DBEM results (a) indicated by the green, dashed line are identical to Fig. 15. *pan*MARE results for the same scenario are shown on the right side (b). Grey lines denote the results of quasi-steady reference simulations of the individual methods. Dotted lines mark the average height of minimum and maximum peaks.

used to simulate the behaviour of the IEA 15-MW and 22-MW wind turbines. Differences of up to 10% could be observed between the FVW and DBEM methods in steady cases. Those were assigned to differences in the modelling approaches. However, a further investigation has not been undertaken, since the impact of unsteady phenomena is the focus of this work. The isolation of these unsteady impacts was achieved with the aid of specialised load case sets covering an extremely large motion period range and a number of wind speeds in the below-rated region of a typical FOWT. A comparison of the unsteady thrust force response of the turbines and methods revealed a number of findings that allowed for a generalisation of the impact of unsteady aerodynamic phenomena. In addition, an investigation of the axial induced velocity gave insights into the way the dynamic wake effect impacts the unsteady behaviour of the thrust force. Five key findings of these analyses are summarised in the following paragraphs.

First, a significant impact of three unsteady phenomena on the thrust force response to surge motions was found for the considered large-scale FOWT. The dynamic wake, unsteady airfoil and returning wake effect caused a reduction of the thrust force amplitude of up to 30% in case of the IEA 15-MW and up to 40% in the case of the IEA 22-MW rotor at realistic motion periods. Further analysis allowed us to separate the impact of the dynamic wake effect and the two remaining effects and to clearly link those to the change of the load response with varying motion periods.

Second, an attempt to generalise the impact of unsteady phenomena on the rotor thrust force in terms of a characteristic curve was presented. The curve consists of four phases: A quasi-steady phase at extremely slow motions, the dynamic wake evolution phase, a plateau phase with fully evolved dynamic wake effect and a fully unsteady phase at high motion frequencies, where all three unsteady effects are active. The motion period ranges corresponding to the phases can be predicted by the dimensionless *rotor reduced frequency*, *airfoil reduced frequency* and *motion to blade passing frequency ratio*. At constant TSR, the characteristic curve can also be expressed in terms of the rotor reduced frequency only, due to the linear dependency between the three dimensionless numbers. The corresponding period ranges for the different phases can then be predicted based on the rotor reduced frequency without prior simulations and can be assumed to be transferable to any typical large-scale wind turbine.

Third, the dynamic wake effect significantly impacts the thrust force response to surge motions, which contrasts findings from previous investigations on model-scale rotors (UNAFOW and TUHH rotors). The motion period range, in which the dynamic wake effect is active, can be predicted by the rotor reduced frequency for the considered turbines. However, the strength of its impact on the thrust force response was found to depend on the turbine and modelling approach. The reduction of the thrust force amplitude induced by the dynamic wake effect was found to be in a range of 15–20% in case of the IEA 22-MW. The present analysis showed that the deviations to the model scale rotors result from differences of the steady behaviour of the axial induced velocity over the TSR. It could be shown that the sensitivity of the axial induced velocity on changes of the TSR is the crucial indicator for predicting the strength of the dynamic wake effect.

Fourth, the two FVW methods predict a very similar impact of the unsteady phenomena on the thrust force, while significant differences arise when comparing those to the DBEM method. A major source of these differences is the returning wake effect, which is not modelled in DBEM methods. At the motion period associated with the peak activity of the returning wake effect, the DBEM calculated a thrust force amplitude of the IEA 22-MW that was damped by only 20%, while the FVW method predicted 40% reduction. In addition, the strength of the dynamic wake effect on the thrust force response was predicted differently by the methods. This was caused by the abovementioned deviations in the steady modelling of the FVW and the DBEM methods rather than different approaches of the unsteady modelling. A comparison of the induced velocity fluctuations during surge motions revealed that the dynamic wake modelling in the DBEM method generally meets the behaviour of the FVW methods but predicts a slightly weaker attenuation.

Fifth, the applicability of the generalised thrust characteristic is demonstrated in a simplified, but realistic scenario. The reduction of rotor thrust fluctuations caused by unsteady phenomena showed good agreement with the unsteady thrust force characteristic determined from harmonic surge motions. This emphasises that the obtained generalised unsteady thrust force characteristic can be applied to predict the impact of unsteady aerodynamic phenomena on real FOWT in motion. Concurrently, it was shown for the first time that the returning wake effect can have a significant influence of the thrust force response of large-scale FOWT in realistic motion conditions.

In conclusion, the dynamic wake effect, unsteady airfoil effect and returning wake effect have to be considered when modelling large-scale FOWT. The occurrence and impact of these individual effects can be predicted with our proposed four-phase model. Our model can be used to determine whether a modelling of the unsteady airfoil and returning

wake effect is necessary in a specific case. Realistic ranges of rotor reduced frequencies lie approximately between 0.5 and 16 for FOWT of the 15 MW class and between 1 to 20 for the 22 MW class. Therefore, unsteady contributions from the dynamic wake effect always need to be considered as it can only be excluded for rotor reduced frequencies far below 1. This is of major importance for future reduced-order models used for control development and hybrid wave tank tests.

Another important field of application of the findings is the simulation and understanding of FOWT wakes. Messmer et al. [1] recently found that the wake recovery of a surging wind turbine can be significantly increased by the formation of coherent structures in an experimental study. In order to reproduce such findings numerically, the rotor thrust oscillations need to be captured accurately. The presented thrust force characteristic could therefore serve as an input for empirical far-wake models. In addition, the linking of the unsteady phenomena to dimensionless numbers in our four-phase-model could help to understand the relation between these phenomena and the increased wake recovery in [1].

Future numerical and experimental studies should increase the range of motion frequencies to reach rotor reduced frequencies above 10 when attempting to cover a realistic motion frequency range. Especially in the case of experimental studies, this will be challenging because they have been limited to rotor reduced frequencies below 2 due to technical limitations. Finally, it has to be noted that the present study was limited to a constant rotational speed. However, a previous work of some of the authors already showed that oscillations of the rotational speed can also cause unsteady behaviour. Future work should therefore investigate to which extent such oscillations are present in realistic environments and characterise the resulting unsteady contributions.

CRediT authorship contribution statement

Christian W. Schulz: Writing – original draft, Visualization, Methodology, Investigation, Formal analysis, Data curation, Conceptualization. **Roger Bergua:** Writing – review & editing, Methodology, Investigation. **Emmanuel Branlard:** Writing – review & editing, Validation, Software. **Stefan Netzband:** Writing – review & editing, Software, Methodology. **Jason Jonkman:** Writing – review & editing, Validation, Software. **Amy Roberston:** Writing – review & editing, Validation.

Declaration of competing interest

The authors declare that they have no known competing financial interests or personal relationships that could have appeared to influence the work reported in this paper.

Acknowledgements

The authors gratefully acknowledge the support of the Federal Ministry for Economic Affairs and Energy (BMWE) for funding the VAMOS project (03EE2004C), the ProHyGen project (03EI3084C) as well as the participation in the IEA Task 30.

This work was authored in part by the National Renewable Energy Laboratory for the U.S. Department of Energy (DOE), operated under Contract No. DE-AC36-08GO28308. Funding provided by U.S. Department of Energy's Office of Energy Efficiency and Renewable Energy and Wind Energy Technologies Office. The views expressed in the article do not necessarily represent the views of the DOE or the U.S. Government. The U.S. Government retains and the publisher, by accepting the article for publication, acknowledges that the U.S. Government retains a nonexclusive, paid-up, irrevocable, worldwide license to publish or reproduce the published form of this work, or allow others to do so, for U.S. Government purposes.

Appendix A. Description of numerical methods

A.1. panMARE FVW

The first-order panel method *pan*MARE, developed at the Hamburg University of Technology (TUHH), has been applied successfully to offshore structures and ship propellers [31] in the past decades. It was expanded by Netzband et al. [32] to enable fully coupled simulations of FOWTs. In this study, only the lifting line module of *pan*MARE is employed to model the rotor aerodynamics. The blade surface is simplified to a lifting line positioned at the quarter-chord point, with the wake shed from the trailing edge. Local inflow velocity and angle of attack are calculated based on the flow field in every iteration, accounting for the effects of the wake and all inflow parameters. Subsequently, the lift and drag of the blade sections are derived from airfoil polars, and the circulation is obtained from the lift force for each blade segment. The Lamb–Oseen vortex core model is applied to avoid singularities in the wake flow field, which are typical for FVW methods. No unsteady corrections for the airfoil aerodynamics, such as a dynamic stall model, are applied. Explicit validations of *pan*MARE's lifting line module were performed with wave tank [33] and wind tunnel experiments [3,4].

A.2. OpenFAST FVW/AeroDyn OLAF

The cOnvecting LAgrangian Filaments (OLAF) module is a free vortex wake method similar to the above described lifting line module of *pan*MARE. It is used to determine the aerodynamic forces acting on two- or three-bladed horizontal-axis wind turbines in motion. OLAF has been integrated into OpenFAST, a physics-based engineering software from the National Renewable Energy Laboratory that models the combined aerodynamic, hydrodynamic, servo, and structural behaviour of individual wind turbines. Within OpenFAST, OLAF functions as part of the AeroDyn module and provides an alternative method to the traditional blade element momentum (BEM) theory.

OLAF represents the turbine blades using a lifting line approach, which involves a distribution of bound circulation along the blade. Changes in this bound circulation over time and space cause the shedding of free vorticity into the wake region behind the turbine. Similar to *pan*MARE, OLAF uses vortex core models to account for the singular behaviour of the vortex filaments. In addition to this, a number of additional corrections accounting for, e.g. vortex diffusion over time are implemented. OLAF also includes a Beddoes–Leishman type unsteady airfoil correction to account for dynamic stall. In contrast to other implementations of this model in BEM methods, the used correction omits the circulatory unsteady airfoil effect in attached flow in order to avoid double counting this effect. Details on the implementation can be found in [34].

A.3. OpenFAST DBEM/AeroDyn DBEM

BEM methods, such as OpenFAST BEM (AeroDyn), are founded on the assumption that momentum equilibrium is achieved independently within each annular ring of a wind turbine rotor. This allows the calculation of rotor loads using airfoil polars corresponding to the airfoils at the respective blade sections. Unlike FVW methods, these approaches do not directly model the flow field in the wake. The DBEM method employed in this work (AeroDyn v15 within OpenFAST) incorporates two unsteady corrections to account for the dynamic inflow effect and the unsteady airfoil effect. The unsteady airfoil correction is derived from a modified version of the Beddoes–Leishman model [13], which also addresses dynamic stall phenomena. Additionally, the dynamic inflow correction, based on Øye's formulation (refer to [35]), serves to prevent abrupt changes in axial induction. More details on AeroDyn as well as the unsteady corrections can be found in [36–38].

Appendix B. Description of numerical setups

B.1. IEA 15-MW rotor models

All geometry parameters and airfoil characteristics of the IEA 15-MW rotor were extracted from the definition document [39] and the official GitHub repository.[24] In *pan*MARE, the blade starts at a relative radius of 5% and is discretised with 30 radial stations containing refinements towards tip and hub. For the OpenFAST FVW model, the discretisation from the repository remains unchanged in order to allow for a straightforward reproduction of the simulations, which results in a uniform distribution of the 50 radial sections representing the complete blade. The time step size in both methods is set individually for the different load cases maintaining a constant rotation angle of 3° per time step. This results in an extremely high number of time steps and wake panels in comparison to typical simulation settings of FVW models. However, such detailed temporal discretisation is necessary, because the aerodynamic behaviour of very low motion periods shall be captured as accurately as possible. The high temporal discretisation results in a very high wake resolution at the chosen wake length (approx. four rotor diameters). This is tackled by three wake coarsening stages in *pan*MARE, where two neighboured wake panels are merged together in tangential direction. In OpenFAST FVW, a reduction of wake panels could be reached by using the far wake model, where the vortices in the wake are considered as concentrated tip and hub vortices only. However, in order to exclude the far wake model as a potential source for differences between the two lifting line methods, the whole wake is treated as near wake in OpenFAST FVW. In addition, the free wake deformation is frozen after 2/3 of a rotor rotation in both setups.

The solver settings of the OpenFAST DBEM model are identical with the ones published in the repository. They include hub and tip loss corrections (Prandtl), the unsteady airfoil correction and the dynamic wake correction. For the unsteady airfoil corrections, the coefficients A_1, A_2, b_1 and b_2 have been estimated for a NACA0012 airfoil [13]. However, these are typically also used for other airfoils. The time constant of the dynamic inflow correction (τ_1) is estimated by an integrated formula based on Øye's approach (see e.g. [38]). All simulations were performed with a time step size of 0.01 s.

B.2. IEA 22-MW rotor models

All geometry parameters and airfoil characteristics of the IEA 22-MW rotor were extracted from the definition document [28] and the official GitHub repository.[25] As blades of this particular turbine are designed with a comparatively small stiffness in the torsional direction, neglecting blade torsion would lead to a very different aerodynamic behaviour, especially near rated wind speed. While blade flexibility shall be excluded from the study, an average twist deviation from the original blade geometry is applied to the rotor models. In order to meet the overall aerodynamic behaviour properly with rigid blades, the twist distribution of the blade is adjusted so that the deformed blade twist distribution obtained in the fully flexible HAWC2 simulations from the repository at a wind speed of 7 ms^{-1} is met.

The *pan*MARE setup is, except for the geometry, nearly identical to the one of the IEA 15-MW rotor. As the rotational speed is a bit lower in the case of the larger rotor, a slightly lower wake discretisation of 3.88° is applied, while the other parameters remain approximately constant. Similarly, the OpenFAST DBEM setup is identical to the one in the repository (apart form the twist distribution) and the solver settings from the IEA 15-MW setup were adopted.

[24] https://github.com/IEAWindTask37/IEA-15-240-RWT, accessed at April 9th, 2025.

[25] https://github.com/IEAWindSystems/IEA-22-280-RWT, accessed at April 9th, 2025.

Appendix C. Extraction of induced velocities

The induced velocity in BEM methods typically only consider velocity components that determine the momentum equilibrium, e.g. an average value over the rotor annulus or part of it. In contrast to this, the induced velocity in FVW methods includes all velocities induced by the wake at the actual blade position. In other words, BEM methods define the induced velocity based on the influence of the trailing vortex system, while FVW methods typically incorporate the complete vortex system including the shed vortices. Therefore, the state of the overall momentum equilibrium (on an annular ring) can be directly evaluated using the axial induced velocity in BEM methods. In the case of FVW methods, the induced velocity also includes velocity fluctuations caused by the unsteady airfoil and returning wake effect, which do not alter the overall momentum equilibrium. When using the axial induction as an indicator for the state of the momentum equilibrium, the definition used in BEM methods seems more useful. This is especially true when investigating the dynamic wake effect, as it impacts induced velocities caused by the trailing vortex system only. Therefore, the rotor averaged induced velocity is chosen as quantity of interest for the investigations in Section 4.4. In the case of the FVW method, this is calculated as follows: The velocity induced by the complete vortex system is extracted on 10 annular rings, which are located at 0.02 D[26] behind the rotor. Their components parallel to the wind direction are then averaged for every ring in every time step. The rotor averaged axial induced velocity is than calculated by an area weighted average of the values corresponding to the annular rings.

Data availability

All used data can be provided on request.

References

[1] T. Messmer, M. Hölling, J. Peinke, Enhanced recovery caused by nonlinear dynamics in the wake of a floating offshore wind turbine, J. Fluid Mech. 984 (2024) A66, http://dx.doi.org/10.1017/jfm.2024.175, URL https://doi.org/10.1017/jfm.2024.175.

[2] T. Messmer, J. Peinke, A. Croce, M. Hölling, The role of motion-excited coherent structures in improved wake recovery of a floating wind turbine, J. Fluid Mech. 1018 (2025) A23, http://dx.doi.org/10.1017/jfm.2025.10509, URL https://doi.org/10.1017/jfm.2025.10509.

[3] C.W. Schulz, S. Netzband, U. Özinan, P.W. Cheng, M. Abdel-Maksoud, Wind turbine rotors in surge motion: new insights into unsteady aerodynamics of floating offshore wind turbines (FOWTs) from experiments and simulations, Wind. Energ Sci. 9 (2024) 665–695, http://dx.doi.org/10.5194/wes-9-665-2024, URL https://wes.copernicus.org/articles/9/665/2024/.

[4] R. Bergua, A. Robertson, J. Jonkman, E. Branlard, A. Fontanella, M. Belloli, P. Schito, A. Zasso, G. Persico, A. Sanvito, E. Amet, C. Brun, G. Campaña-Alonso, R. Martín-San-Román, R. Cai, J. Cai, Q. Qian, W. Maoshi, A. Beardsell, G. Pirrung, N. Ramos-García, W. Shi, J. Fu, R. Corniglion, A. Lovera, J. Galván, T.A. Nygaard, C.R. dos Santos, P. Gilbert, P.-A. Joulin, F. Blondel, E. Frickel, P. Chen, Z. Hu, R. Boisard, K. Yilmazlar, A. Croce, V. Harnois, L. Zhang, Y. Li, A. Aristondo, I. Mendikoa Alonso, S. Mancini, K. Boorsma, F. Savenije, D. Marten, R. Soto-Valle, C.W. Schulz, S. Netzband, A. Bianchini, F. Papi, S. Cioni, P. Trubat, D. Alarcon, C. Molins, M. Cormier, K. Brüker, T. Lutz, Q. Xiao, Z. Deng, F. Haudin, A. Goveas, OC6 project phase III: validation of the aerodynamic loading on a wind turbine rotor undergoing large motion caused by a floating support structure, Wind. Energ Sci. 8 (2023) 465–485, http://dx.doi.org/10.5194/wes-8-465-2023, URL https://wes.copernicus.org/articles/8/465/2023/.

[5] A. Fontanella, A. Fusetti, S. Cioni, F. Papi, S. Muggiasca, G. Persico, V. Dossena, A. Bianchini, M. Belloli, Wake development in floating wind turbines: New insights and open dataset from wind tunnel experiments, Wind. Energy Sci. Dis. (2024) 1–23, http://dx.doi.org/10.5194/wes-2024-140, (Preprint) URL https://wes.copernicus.org/preprints/wes-2024-140/.

[26] This is an arbitrary choice. However, the sensitivity of the extracted velocity to this parameter is comparatively small.

[6] F. Taruffi, F. Novais, A. Viré, An experimental study on the aerodynamic loads of a floating offshore wind turbine under imposed motions, Wind. Energ Sci. 9 (2024) 343–358, http://dx.doi.org/10.5194/wes-9-343-2024, URL https://wes.copernicus.org/articles/9/343/2024/.

[7] F. Taruffi, R. Combette, A. Viré, Experimental and cfd analysis of a floating offshore wind turbine under imposed motions, J. Phys.: Conf. Ser. 2767 (2024) 062010, http://dx.doi.org/10.1088/1742-6596/2767/6/062010, URL https://doi.org/10.1088/1742-6596/2767/6/062010.

[8] T.T. Tran, D.-H. Kim, A CFD study into the influence of unsteady aerodynamic interference on wind turbine surge motion, Renew. Energ 90 (2016) 204–228, http://dx.doi.org/10.1016/j.renene.2015.12.013, URL https://www.sciencedirect.com/science/article/pii/S0960148115305188.

[9] F. Papi, J. Jonkman, A. Robertson, A. Bianchini, Going beyond BEM with BEM: an insight into dynamic inflow effects on floating wind turbines, Wind Energ Sci. (2024) 1069–1088, http://dx.doi.org/10.5194/wes-9-1069-2024, URL https://Wes.Copernicus.Org/Articles/9/1069/2024/.

[10] C.W. Schulz, U. Özinan, S. Netzband, P.W. Cheng, M. Abdel-Maksoud, The impact of unsteadiness on the aerodynamic loads of a floating offshore wind turbine, J. Phys.: Conf. Ser. 2626 (2023) 012064, http://dx.doi.org/10.1088/1742-6596/2626/1/012064, URL https://iopscience.iop.org/article/10.1088/1742-6596/2626/1/012064.

[11] L. Zhou, X. Shen, L. Ma, J. Chen, H. Ouyang, Z. Du, Unsteady aerodynamics of the floating offshore wind turbine due to the trailing vortex induction and airfoil dynamic stall, Energy 304 (2024) 131845, http://dx.doi.org/10.1016/j.energy.2024.131845, URL https://linkinghub.elsevier.com/retrieve/pii/S0360544224016189.

[12] A.G. Sanvito, A. Firpo, P. Schito, V. Dossena, A. Zasso, G. Persico, Insights into the dynamic induction in fowt surge motion using an actuator-line model, J. Phys.: Conf. Ser. 2767 (2024) 052064, http://dx.doi.org/10.1088/1742-6596/2767/5/052064, URL https://doi.org/10.1088/1742-6596/2767/5/052064.

[13] J.G. Leishman, T.S. Beddoes, A semi-empirical model for dynamic stall, J. Am. Helicopter Soc. 34 (1989) 3–17, http://dx.doi.org/10.4050/JAHS.34.3.3.

[14] C. Ferreira, W. Yu, A. Sala, A. Viré, Dynamic inflow model for a floating horizontal axis wind turbine in surge motion, Wind. Energ Sci. 7 (2022) 469–485, http://dx.doi.org/10.5194/wes-7-469-2022, URL https://wes.copernicus.org/articles/7/469/2022/.

[15] T. Sebastian, M. Lackner, Characterization of the unsteady aerodynamics of offshore floating wind turbines, Wind. Energ 16 (2013) 339–352, http://dx.doi.org/10.1002/we.545, URL https://onlinelibrary.wiley.com/doi/abs/10.1002/we.545.

[16] Y. Cai, X. Li, S. Leng, H. Zhao, Y. Zhou, Effect of combined surge and pitch motion on the aerodynamic performance of floating offshore wind turbine, Ocean Eng. 306 (2024) 118061, http://dx.doi.org/10.1016/j.oceaneng.2024.118061, URL https://www.sciencedirect.com/science/article/pii/S0029801824013994.

[17] R. Kyle, Y.C. Lee, W.-G. Früh, Propeller and vortex ring state for floating offshore wind turbines during surge, Renew. Energ 155 (2020) 645–657, http://dx.doi.org/10.1016/j.renene.2020.03.105, URL https://www.sciencedirect.com/science/article/pii/S0960148120304377.

[18] J. Dong, A. Viré, Z. Li, Analysis the vortex ring state and propeller state of floating offshore wind turbines and verification of their prediction criteria by comparing with a CFD model, Renew. Energ 184 (2022) 15–25, http://dx.doi.org/10.1016/j.renene.2021.11.053, URL https://www.sciencedirect.com/science/article/pii/S0960148121016359.

[19] A.F.P. Ribeiro, D. Casalino, C.S. Ferreira, Nonlinear inviscid aerodynamics of a wind turbine rotor in surge, sway, and yaw motions using a free-wake panel method, Wind. Energ Sci. 8 (2023) 661–675, http://dx.doi.org/10.5194/wes-8-661-2023, URL https://wes.copernicus.org/articles/8/661/2023/.

[20] F. Papi, Y. Perignon, A. Bianchini, Derivation of met-ocean conditions for the simulation of floating wind turbines: a European case study, J. Phys.: Conf. Ser. 2385 (2022) 012117, URL https://doi.org/10.1088/1742-6596/2385/1/012117.

[21] G. Ramachandran, A. Robertson, J. Jonkman, M. Masciola, Investigation of response amplitude operators for floating offshore wind turbines, in: 23rd International Ocean and Polar Engineering Conference, 2013, URL https://docs.nrel.gov/docs/fy13osti/58098.pdf.

[22] V. Leroy, S. Delacroix, A. Merrien, E.E. Bachynski-Polić, J.C. Gilloteaux, Experimental investigation of the hydro-elastic response of a spar-type floating offshore wind turbine, Ocean Eng. 255 (2022) 111430, http://dx.doi.org/10.1016/j.oceaneng.2022.111430, URL https://www.sciencedirect.com/science/article/pii/S0029801822008113.

[23] C. Allen, A. Viscelli, H. Dagher, A. Goupee, E. Gaertner, N. Abbas, M. Hall, G. Barter, Definition of the UMaine VolturnUS-S reference platform developed for the IEA wind 15-megawatt offshore reference wind turbine, Technical Report NREL/TP–(1660) 5000-76773012, MainId:9434, 2020, http://dx.doi.org/10.2172/1660012, URL https://www.osti.gov/servlets/purl/1660012/.

[24] F. Trigaux, P. Chatelain, G. Winckelmans, Investigation of blade flexibility effects on the loads and wake of a 15-MW wind turbine using a flexible actuator line method, Wind. Energ Sci. 9 (2024) 1765–1789, http://dx.doi.org/10.5194/wes-{{9}}-1765-2024, URL https://wes.copernicus.org/articles/{{9}}/{1765}/{2024}/.

[25] R. Behrens de Luna, S. Perez-Becker, J. Saverin, D. Marten, F. Papi, M.-L. Ducasse, F. Bonnefoy, A. Bianchini, C.-O. Paschereit, Quantifying the impact of modeling fidelity on different substructure concepts for floating offshore wind turbines – part 1: Validation of the hydrodynamic module QBlade-Ocean, Wind. Energ Sci. 9 (2024) 623–649, http://dx.doi.org/10.5194/wes-9-623-2024, URL https://wes.copernicus.org/articles/9/623/2024/.

[26] J.G. Leishman, Principles of Helicopter Aerodynamics, first ed., Cambridge University Press, 2000.

[27] B. Wen, X. Tian, X. Dong, Z. Peng, W. Zhang, Influences of surge motion on the power and thrust characteristics of an offshore floating wind turbine, Energy 141 (2017) 2054–2068, http://dx.doi.org/10.1016/j.energy.2017.11.090, URL https://linkinghub.elsevier.com/retrieve/pii/S0360544217319485.

[28] F. Zahle, A. Barlas, K. Loenbaek, P. Bortolotti, D. Zalkind, L. Wang, C. Labuschagne, L. Sethuraman, G. Barter, Definition of the IEA wind 22-megawatt offshore reference wind turbine, Technical Report, Technical University of Denmark, 2024, http://dx.doi.org/10.11581/DTU.00000317, URL https://www.osti.gov/biblio/2337779.

[29] F. Vigara, L. Cerdán, R. Durán, S. Muñoz, M. Lynch, S. Doole, C. Molins, P. Trubat, R. Guanche, COREWIND D1.2 design basis, in: Technical Report D1.2, 2019, http://dx.doi.org/10.3030/{815083}.

[30] P. Gómez, G. Sánchez, A. Llana, G. Gonzalez, Lifes50+ deliverable 1.1 Oceanographic and meteorological conditions for the design, Technical Report, 2015, http://dx.doi.org/10.3030/640741.

[31] M. Bauer, M. Abdel-Maksoud, A 3-d potential based boundary element method for modelling and simulation of marine propeller flows, in: IFAC Proceedings Volumes, in: 7th Vienna International Conference on Mathematical Modelling, volume 45, 2012, pp. 1179–1184, http://dx.doi.org/10.3182/20120215-3-AT-3016.00209, URL https://www.sciencedirect.com/science/article/pii/S1474667016308424.

[32] S. Netzband, C.W. Schulz, U. Göttsche, D. Ferreira González, M. Abdel-Maksoud, A panel method for floating offshore wind turbine simulations with fully integrated aero- and hydrodynamic modelling in time domain, Ship Technol. Res. 65 (2018) 123–136, http://dx.doi.org/10.1080/09377255.2018.1475710.

[33] C.W. Schulz, S. Netzband, P.D. Knipper, M. Abdel-Maksoud, Low-uncertainty wave tank testing and validation of numerical methods for floating offshore wind turbines, Wind. Energ Sci. 9 (2024) 1941–1965, http://dx.doi.org/10.5194/wes-9-1941-2024, URL https://wes.copernicus.org/articles/9/1941/2024/.

[34] K. Shaler, E. Branlard, A. Platt, OLAF user's guide and theory manual, Technical Report NREL/TP-(1659) 5000-75959853, MainId:6799, 2020, http://dx.doi.org/10.2172/1659853, URL https://www.osti.gov/servlets/purl/1659853/.

[35] H. Snel, J.G. Schepers, G.J.W. van Bussel, L.J. Vermeer, R.I. Rawlinson Smith, S. Voutsinas, T. van Holten, S. Oye, R. Bareiß, Joint investigation of dynamic inflow effects and implementation of an engineering method, Technical Report ECN-C-94-107, Netherlands Energy Research Center, 1995.

[36] P.J. Moriarty, A.C. Hansen, AeroDyn theory manual, Technical Report NREL/TP-500-36881, National Renewable Energy Lab. Golden, CO (US), 2005, http://dx.doi.org/10.2172/15014831, URL https://www.osti.gov/biblio/15014831.

[37] R.R. Damiani, G. Hayman, The unsteady aerodynamics module for FAST8, Technical Report NREL/TP–(1576) 5000-66347488, National Renewable Energy Lab. (NREL), Golden, CO (United States), http://dx.doi.org/10.2172/1576488.

[38] E. Branlard, B. Jonkman, G.R. Pirrung, K. Dixon, J. Jonkman, Dynamic inflow and unsteady aerodynamics models for modal and stability analyses in openfast, J. Phys: Conf. Ser. 2265 (2022) 032044, http://dx.doi.org/10.1088/1742-6596/2265/3/032044, URL https://iopscience.iop.org/article/10.1088/1742-6596/2265/3/032044.

[39] E. Gaertner, J. Rinker, L. Sethuraman, F. Zahle, B. Anderson, G.E. Barter, N.J. Abbas, F. Meng, P. Bortolotti, W. Skrzypinski, G.N. Scott, R. Feil, H. Bredmose, K. Dykes, M. Shields, C. Allen, A. Viselli, IEA wind TCP task 37: Definition of the IEA 15-megawatt offshore reference wind turbine, Technical Report NREL/TP-5000-75698, National Renewable Energy Lab. (NREL), Golden, CO (United States), 2020, http://dx.doi.org/10.2172/1603478, URL https://www.osti.gov/biblio/1603478.